Check for updates

Microglia phagocytose myelin sheaths to modify developmental myelination

Alexandria N. Hughes [1] and Bruce Appel [2] ✉

During development, oligodendrocytes contact and wrap neuronal axons with myelin. Similarly to neurons and synapses, excess myelin sheaths are produced and selectively eliminated, but how elimination occurs is unknown. Microglia, the resident immune cells of the central nervous system, engulf surplus neurons and synapses. To determine whether microglia also prune myelin sheaths, we used zebrafish to visualize and manipulate interactions between microglia, oligodendrocytes, and neurons during development. We found that microglia closely associate with oligodendrocytes and specifically phagocytose myelin sheaths. By using a combination of optical, genetic, chemogenetic, and behavioral approaches, we reveal that neuronal activity bidirectionally balances microglial association with neuronal cell bodies and myelin phagocytosis in the optic tectum. Furthermore, multiple strategies to deplete microglia resulted in oligodendrocytes maintaining excessive and ectopic myelin. Our work reveals a neuronal activity-regulated role for microglia in modifying developmental myelin targeting by oligodendrocytes.

Neuronal axon conduction velocity is supported by myelin, a specialized, proteolipid-rich membrane produced by glial cells. During development, oligodendrocytes generate numerous nascent myelin sheaths along axons. Neuronal activity promotes the formation and maturation of myelin sheaths[1–3] and can bias which axons are selected for myelination[1,4]. Sensory enrichment and deprivation paradigms in both mice and humans can modify oligodendrogenesis and myelination in relevant brain regions[5–7], raising the possibility that changes in myelin support the development of higher cognitive functions. Consistent with this possibility, new myelin is required for at least some types of learning[8].

An underappreciated dimension of myelin plasticity is myelin elimination. Similar to neurons and synapses of the developing central nervous system (CNS), myelin is first overproduced and then partially eliminated[9]. How myelin sheaths are removed is unknown. Microglia, the resident immune cell type of the CNS, eliminate surplus neurons and synapses during development. Microglia detect and respond to neuronal activity[10,11], notably engulfing synapses in an activity-regulated manner to direct development of the visual system[12]. In neurological and neurodegenerative diseases, this synaptic elimination program can re-emerge maladaptively to promote disease progression[13]. Notably, microglial phagocytosis of myelin is also a feature of neural disease and injury[14,15]. Therefore, to explain developmental myelin elimination, we hypothesized that microglia engulf myelin sheaths during development to sculpt myelination.

To test this hypothesis, we manipulated and directly observed interactions between microglia, myelin, and neurons in vivo using zebrafish as a model system. We found that microglia are intimately associated with oligodendrocytes and specifically phagocytose myelin sheaths, leaving cell bodies intact. We used multiple strategies to manipulate neuronal activity and demonstrated that microglia are attracted to active neurons at the expense of myelin phagocytosis and, conversely, microglia phagocytose more myelin and contact fewer neurons when neuronal activity is silenced. By eliminating microglia, we found evidence that microglia remove excess myelin sheaths and prevent ectopic myelination of cell bod-ies. Our data establish that microglia limit developmental myelination and thereby extend our understanding of the mechanistic basis of myelin plasticity.

Results

Microglia survey myelinated axon tracts. Our first objective was to determine whether a relationship exists between microglia and oligodendrocytes during development. To visualize microglia, we established a transgenic line of zebrafish, *Tg(mpeg1.1:mVenus-CAAX)*, in which *mpeg1.1* regulatory DNA drives expression of membrane-tethered mVenus-CAAX in microglia and macrophages. Crossing this line to animals carrying *Tg(mbpa:mCherry-CAAX)*, a transgene that labels myelinating oligodendrocyte membrane with mCherry, permitted us to see microglia–oligodendrocyte interactions (Fig. 1a). In the spinal cord at 4 d postfertilization (d.p.f.), the time at which *Tg(mbpa:mCherry-CAAX)* expression becomes visible, spinal cord microglia almost exclusively occupied the myelinated tracts of the dorsal and medial longitudinal fasciculi. By counting microglia in each of these tracts over developmental time, we found that microglia had an early bias for localization in the medial longitudinal fasciculus of the ventral spinal cord but occupied the tracts equally by 8 d.p.f. (Fig. 1b). To learn whether the change in microglia distribution correlates with a change in oligodendrocyte number, we counted oligodendrocyte cell bodies in dorsal and ventral tracts in a 3.5-hemisegment region. Similarly to microglia, oligodendrocytes were initially more numerous in the ventral tract but became more equally distributed between tracts by 8 d.p.f. (Fig. 1c,d). Comparing the dorsal to ventral ratio of oligodendrocytes and microglia revealed that they were nearly evenly matched in both locations over developmental time (Fig. 1e). Because microglia are motile cells, we sought to determine the extent of their surveillance of the myelinated tracts. To accomplish this, we performed timelapse imaging of the spinal cord and assessed the frequency of microglia migrating through a 3.5-hemisegment region. We found that regions were visited by a migrating microglia roughly every 4 h (Fig. 1f,g). These observations reveal that spinal cord microglia associate with oligodendrocytes during development, and suggest

[1]Neuroscience Graduate Program, University of Colorado, Aurora, CO, USA. [2]Department of Pediatrics, Section of Developmental Biology, University of Colorado, Aurora, CO, USA. ✉e-mail: bruce.appel@cuanschutz.edu

that microglia are sufficiently motile to comprehensively survey myelinated axon tracts.

We next assessed how microglia interact with oligodendrocytes. During larval stages, microglia have few, mostly primary, processes. We determined that most processes associated with myelin sheaths rather than oligodendrocyte cell bodies or putative targets unlabeled by our transgenic reporters (Fig. 1h–j). Timelapse imaging revealed that microglia processes were not static but were continually retracted and extended within myelinated tracts labeled by *Tg(sox10:mRFP)* (Fig. 1k,l). These dynamic behaviors are consistent with the possibility that microglia survey a large fraction of nascent myelin sheaths in the spinal cord.

Microglia phagocytose myelin sheaths but not oligodendrocytes.
To learn whether myelin-associated microglia are phagocytic, we performed imaging experiments to detect intracellular calcium transients, a signature of phagocytic microglia and macrophages[16,17]. To visualize calcium dynamics, we generated a transgenic line, *Tg(mpeg1.1:GCaMP6s-CAAX)*, which labels microglia membrane with the calcium indicator GCaMP6s-CAAX. By imaging microglia in 4 d.p.f. larvae, we found numerous spontaneous calcium events within process tips, branches and the cell body. To distinguish calcium transients from membrane fluctuations that occur during cellular movement, we imaged microglia in larvae carrying both GCaMP6s-CAAX and another membrane-tethered fluorophore, mScarlet-CAAX, at 4 d.p.f., and detected and investigated events with the calcium imaging toolbox AQuA (Fig. 2a). We found that calcium events were distinguishable from membrane movement events on the basis of fluorescence change, dF/F (Fig. 2b), so we set a threshold for calcium events to include only those with $dF/F > 0.05$. By this criterion, 100% of microglia exhibited calcium transients during a 10-min acquisition (Supplementary Table 1). To determine whether these calcium events represent phagocytic activity at microglia–myelin contacts, we next performed calcium imaging on *Tg(mpeg1.1:GCaMP6s-CAAX; sox10:mRFP)* larvae (Fig. 2c and Supplementary Videos 1 and 2). Microglia exhibited transients both within processes contacting sheaths and those not contacting sheaths. Of the 645 filtered calcium events we detected in 31 microglia, we further filtered events to examine the sheath-contacting status of the largest calcium events ($dF/F > 0.10$, area $> 3\,\mu m^2$), which yielded 41 events in 9/31 cells. These events predominantly occurred at contacts with myelin sheaths (Fig. 2d) and were distinguishable from non-sheath-contacting events on the basis of event duration (Fig. 2e and Extended Data Fig. 1), consistent with these events representing a specific signaling program within sheath-contacting processes. Indeed, we found that sheath-contacting processes exhibiting calcium transients were sometimes followed by sheath disappearance (Fig. 2f and Supplementary Videos 3 and 4), consistent with calcium signaling as a signature of phagocytic activity.

To investigate phagocytosis of myelin sheaths directly, we next performed timelapse imaging in 4 d.p.f. *Tg(mpeg1.1:mVenus-CAAX; sox10:mRFP)* larvae. Similar to our observations of apparent sheath loss following calcium events (Fig. 2f), our timelapse imaging experiments captured occasional whole-sheath engulfment events by microglia (Fig. 2g and Supplementary Video 5). To determine the relative proportion of sheaths eliminated by engulfment and retraction, we performed timelapse imaging of microglia and their surrounding 3.5-hemisegment territory for 3 h. To identify sheaths that disappeared during timelapse in a semiautomatic and unbiased way, we used the myelin channel frames to generate a series of images in which the exclusive-or (XOR) operation is performed on consecutive frames, creating a series of signals that change over time (see Methods and Supplementary Table 2). Summing these XOR frames and merging with the time-summed myelin channel identified sheaths that disappeared over time, while keeping us blinded to microglial location and thus sheath association (Fig. 2h). Tagged sheaths were then tracked in the original timelapse to detect microglial engulfment or lack of microglial contact (retraction). We found that, although both engulfment and retraction contribute to sheath elimination, microglial engulfment accounted for the majority (~70%) of sheath elimination at this stage (Fig. 2i,j). Furthermore, sheaths engulfed by microglia were longer than those that were retracted (Fig. 2k), raising the possibility that engulfment targets more mature sheaths. Consistent with this possibility, timelapse imaging of microglia interacting with *mbpa⁺* oligodendrocytes revealed similar sheath engulfment (Fig. 2l). We validated these observations of myelin phagocytosis using an alternative method to visualize myelin within microglia. Specifically, we performed immunohistochemistry to detect myelin basic protein (Mbp) in tissue obtained from *Tg(mpeg1.1:mVenus-CAAX; mbpa:mCherry-CAAX)* larvae. Nearly all mCherry-CAAX inclusions in microglia were Mbp⁺, indicating that mCherry-CAAX inclusions represent phagocytosed myelin in living larvae (Fig. 2m,n and Extended Data Fig. 2).

Following engulfment, fluorescent material was only briefly visible within microglia before fluorescence disappeared, limiting our ability to estimate the fraction of microglia that phagocytose myelin during development (Fig. 3a). This rapid disappearance probably results from degradation by phagosome acidification. We therefore predicted that inhibiting the acidification of phagosomes would delay the breakdown of phagocytosed myelin and allow us to determine the fraction of microglia that phagocytose myelin membrane

Fig. 1 | Microglia dynamically engage with myelin sheaths in the spinal cord. a, Lateral tile scans of spinal cords of *Tg(mpeg1.1:mVenus-CAAX; mbpa:mCherry-CAAX)* larvae at 4, 5 and 8 d.p.f. Closed arrowheads mark microglia and open arrowheads mark peripheral macrophages. Scale bar, 50 μm. **b**, Microglia counts in dorsal and ventral tracts (hemicord) in 4, 5 and 8 d.p.f. larvae. Wilcoxon rank-sum test, *n* = fish/cells, *n* = 10/60 4 d.p.f., 17/109 5 d.p.f., 13/97 8 d.p.f. **c**, Oligodendrocytes in 3.5 hemisegments in the spinal cord of *Tg(mbpa:TagRFP-T)* larvae at 4, 5 and 8 d.p.f. Scale bar, 10 μm. **d**, Oligodendrocyte counts in dorsal and ventral tracts (3.5 hemisegments) in 4, 5 and 8 d.p.f. larvae. Wilcoxon rank-sum test, *n* = fish/cells, *n* = 14/602 4 d.p.f., 11/448 5 d.p.f., 10/482 8 d.p.f. **e**, Ratios of dorsal/ventral cell counts for *mbpa⁺* oligodendrocytes and *mpeg1.1⁺* microglia at 4, 5 and 8 d.p.f., for cells counted in **b**,**d**. Data in **b**,**d**,**e** were analyzed by Wilcoxon rank-sum test. **f**, Timelapse imaging frames over 10 h in *Tg(mpeg1.1:mVenus-CAAX; sox10:mRFP)* larvae at 4 d.p.f. **g**, Time between microglia visits. Each point represents the timelapse acquisition time divided by the number of microglia visits to the imaging field of view in one larva (*n* = 22 larvae). Violin plot lines mark quantiles (25th, 50th and 75th percentiles) and colors are immaterial. **h**, A microglia (yellow) in the dorsal spinal cord of a *Tg(mpeg1.1:mVenus-CAAX;mbpa:mCherry-CAAX)* larva. Closed arrowheads mark close associations of microglial processes with myelin sheaths (magenta rectangles); open arrowheads mark processes extending toward unlabeled targets; dashed box shows a process enveloping a sheath. **i**, Distribution of microglial processes per cell associated with myelin sheaths, oligodendrocyte (OL) somas or unlabeled targets for *n* = 11 cells (11 fish). **j**, Fraction of microglial processes in **i** plotted per target type; Wilcoxon rank-sum test with Bonferroni–Holm correction for multiple comparisons. Each point represents one microglia. **k**, Timelapse imaging frames of a microglia in a *Tg(mpeg1.1:mVenus-CAAX; sox10:mRFP)* larva, pseudocolored to show cell morphology at three different time points and merged. Striped arrowhead marks a process present at 0′ that is absent at 51′ (initial, withdrawn); open arrowhead marks a process generated during the imaging period that later disappears (new, withdrawn); closed arrowhead marks a process that is generated during the imaging period and is maintained at the end of the imaging window (new). **l**, Number of processes generated and withdrawn by microglia during 1 h of timelapse imaging; black trace is the mean (*n* = 14 microglia in 14 fish). Scale bars, 10 μm.

(Fig. 3a,b). To inhibit phagosome acidification, we treated 4 d.p.f. larvae with bafilomycin A1 for 1 h before imaging. Microglia in *Tg(mpeg1.1:mVenus-CAAX; mbpa:mCherry-CAAX)* larvae treated with bafilomycin had more and brighter myelin inclusions than those of larvae treated with vehicle (Fig. 3b). We confirmed that

myelin inclusions were contained within microglia by viewing cells three-dimensionally (Supplementary Video 6). Morphological segmentation allowed us to obtain measurements of these inclusions (Fig. 3c). We found that when larvae were treated with DMSO control, myelin inclusions were evident in about two-thirds of all
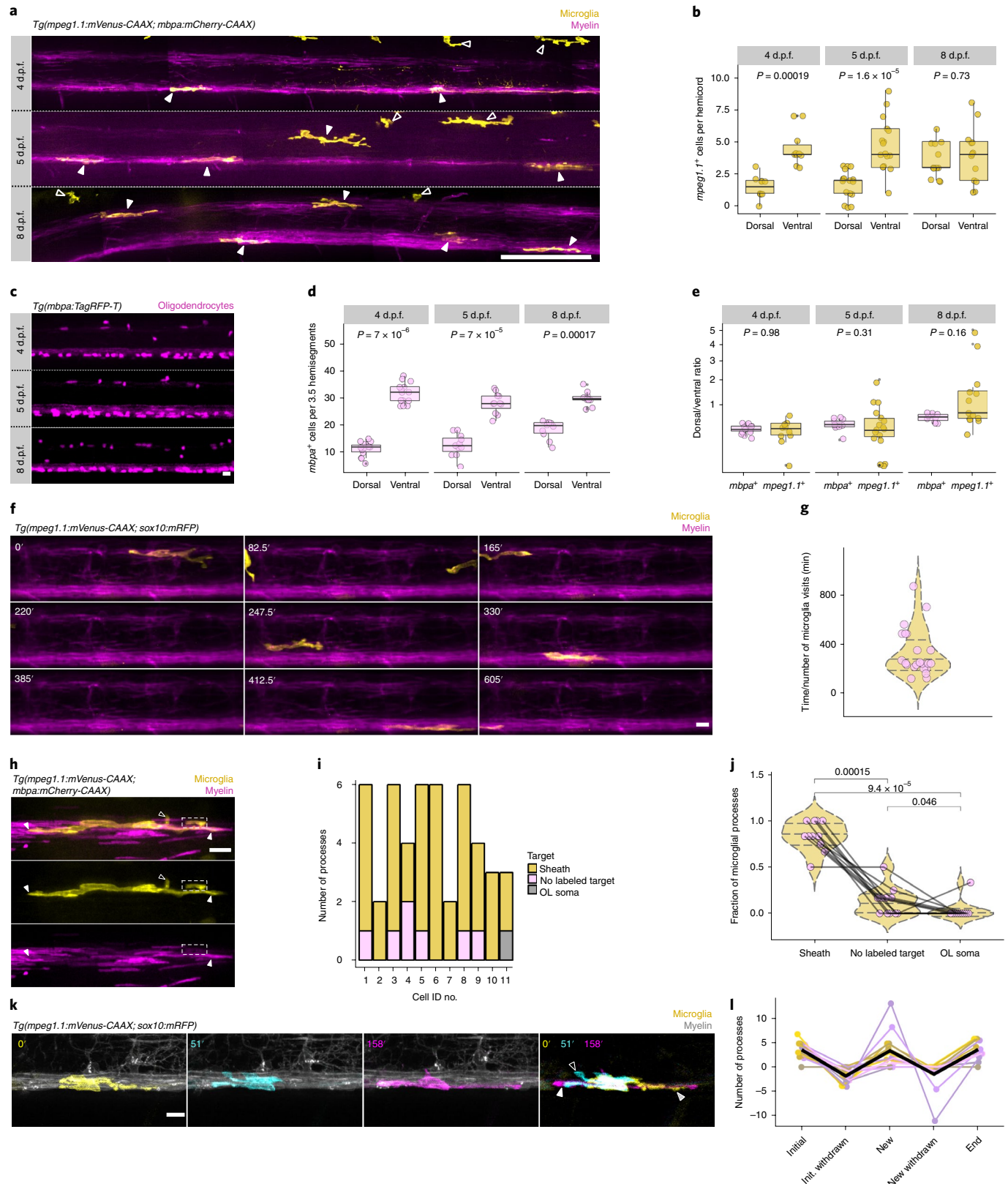
microglia, with the remaining one-third containing no detectable inclusions. However, treatment with bafilomycin to cause acute delay in myelin breakdown revealed that all microglia contained myelin inclusions, suggesting that all spinal cord microglia participate in myelin pruning by phagocytosis (Fig. 3d). Bafilomycin did not change the area of individual inclusions (Fig. 3e) but the total area of inclusions per microglia was increased (Fig. 3f), consistent with stalled myelin breakdown within microglia. Because oligodendrocytes can start myelinating at any time between 4 and 8 d.p.f., we also tested whether myelin phagocytosis detectable by bafilomycin might change over developmental time. We found no difference in the number of myelin inclusions per microglia at 4, 5 or 8 d.p.f., consistent with continuous myelin pruning by microglia over the course of developmental myelination (Fig. 3g).

Although we observed microglial phagocytosis of only individual myelin sheaths, in principle microglia might also engulf entire oligodendrocytes. To investigate this possibility, we first labeled oligodendrocytes undergoing apoptosis using the vital dye acridine orange (Fig. 3h). We found that $mbpa^+$ oligodendrocyte apoptosis was rare and that the frequency was not changed by bafilomycin (Fig. 3h–k and Extended Data Fig. 3). Therefore, dying oligodendrocytes are probably not the source of mCherry-CAAX inclusions in microglia. Next, we tested the possibility that microglia engulf entire live oligodendrocytes. To do so, we repeated our mCherry-CAAX engulfment experiments using an additional oligodendrocyte reporter line, $Tg(mbpa:TagRFP-T)$, in which the same $mbpa$ regulatory DNA drives expression of cytosolic TagRFP-T. Because most oligodendrocyte cytosol is extruded from myelin sheaths, this line primarily labels oligodendrocyte cell bodies (Fig. 3l). We predicted that, if microglia phagocytose entire oligodendrocytes, this oligodendrocyte somatic label would also be detectable within microglia. However, we very rarely detected TagRFP-T within microglia in DMSO- or bafilomycin-treated larvae (Fig. 3m,n). These data suggest that microglia specifically engulf myelin sheaths, with negligible phagocytosis of oligodendrocyte cell bodies.

Myelin phagocytosis is bidirectionally regulated by neuronal activity. Microglia contact numerous myelin sheaths (Fig. 1h–l) but do not phagocytose all sheaths. What determines the amount of myelin phagocytosed by microglia? Previous data showed that neuronal activity can both promote and suppress microglial interactions with cellular targets. For example, active neuronal cell bodies were more frequently contacted by microglia in zebrafish optic tectum[10]. By contrast, inhibition of retinal ganglion cell activity increased microglial engulfment of synapses from axons projecting to lateral geniculate nucleus[12]. Together, these observations suggest that elevated neuronal activity can shift microglia away

from interaction with synapses and toward neuronal cell bodies. We therefore hypothesized that neuronal activity similarly tunes microglial interaction with neuronal cell bodies and myelinated axons, thereby regulating myelin sheath phagocytosis by microglia. To test this, we investigated microglia in the periventricular neuronal cell body layer of optic tectum (Fig. 4a). Approximately ten microglia occupy the cell body layer of each tectal hemisphere[18], positioned between the somas of unmyelinated periventricular neurons and a separate population of heavily myelinated axons that comprise the tectal commissure[19] (Fig. 4a and Supplementary Video 7). We thus tested the possibility that microglia interacting with active neuronal somas would be less likely to phagocytose myelin from the commissural axons and, conversely, that silencing of cell body layer somas would predispose microglia to interact with and phagocytose commissural myelin.

We first tested the effects of manipulation of neuronal activity on microglial interactions with neuronal somas. To do so, we silenced a subset of cell body layer neurons marked by fluorescent protein expression. Specifically, we injected one-cell-stage $Tg(mpeg1.1:mVenus-CAAX; mbpa:mCherry-CAAX)$ embryos with a plasmid designed to bicistronically express either dominant-negative Vamp2 (dnVamp2), a variant lacking the transmembrane domain, or botulinum toxin (BoNT/B) with mTagBFP-CAAX under the control of a pan-neuronal driver. As a control, we mosaically labeled neurons with mTagBFP-CAAX alone. Because expression was mosaic pan-neuronal, we excluded larvae in which tectal commissure axons were labeled so that we could specifically test the role of cell body layer inhibition. We acquired z-stack confocal images of the tectal cell body layer at 4 d.p.f. and determined the fraction of labeled neuronal somas contacted by microglia (Fig. 4b). Whereas neuronal inhibition did not change the number of microglia, microglia made fewer contacts on the cell bodies of inhibited neurons than on control neurons (Fig. 4c,d), consistent with the possibility that reduction of neuronal activity reduces microglial interaction with somas.

To determine whether neuronal activity biases microglia to contact somas, we mosaically activated cell body layer neurons by expressing the capsaicin-gated channel, TRPV1 (*Rattus norvegicus*) fused to mTagBFP in $Tg(mpeg1.1:mVenus-CAAX)$ larvae. At 4 d.p.f. we treated larvae for 2 h either with capsaicin (1 μM) to activate neurons expressing the channel or with DMSO as a control, and then determined the fraction of TRPV1-mTagBFP+ neurons contacted by microglia. Neurons activated by capsaicin more frequently received somatic contact by microglia (Fig. 4e,f), despite an unchanged number of available microglia (Fig. 4g). To learn how microglia acutely respond to soma activation, we locally increased neuronal activity in the cell body layer by photo-uncaging MNI-glutamate (Fig. 4h). We determined that our

Fig. 2 | Microglia phagocytose myelin sheaths during developmental myelination. a, Timelapse imaging (left) and AQuA transient detection in a microglia carrying dual reporters for membrane fluorescence (mScarlet-CAAX) and membrane calcium (GCaMP6s-CAAX) (right). Open arrowheads label membrane events present in both channels; closed arrowheads mark calcium transients. **b**, Histogram of membrane and calcium event dF/F values (649 calcium events in 31 cells, 228 membrane events in 9 cells) showing that events are separable by dF/F; therefore, only events with dF/F > 0.05 were considered calcium transients. a.u., arbitrary units. **c**, Timelapse imaging of filtered calcium transients (dF/F > 0.05) in a microglia interacting with myelin. Closed arrowheads mark events occurring at points of contact with sheaths; open arrowheads mark events at non-sheath-contacting processes. **d,e**, Fraction of large calcium events (**d**) and event duration (**e**) associated with sheath-contacting and non-contacting processes. Wilcoxon rank-sum test, $n = 32/9$ filtered events from 9 cells/9 fish. **f**, Timelapse imaging of a microglia calcium transient and phagocytosis of contacted material (arrowhead marks blebbing; asterisk marks loss of signal). **g**, Timelapse imaging of a microglia engulfing a nascent myelin sheath. **h**, Analysis scheme for detection of myelin sheaths eliminated by phagocytosis or retraction. Timelapse frames (left) are processed by consecutive XOR calculation to generate an image of lost sheaths (cyan); those engulfed by microglia are engulfed (closed arrowhead), whereas those lost but not contacted are retracted. **i**, Paired comparison of number of sheaths lost by engulfment and retraction over 3 h in 30 microglia from 30 animals. Each pair-connected line represents one animal; Wilcoxon rank-sum test. **j**, Relative fractions of sheaths across all timelapse acquisitions that were engulfed or retracted. **k**, Lengths of sheaths eliminated by engulfment versus retraction; Wilcoxon rank-sum test ($n = 135$ sheaths from 30 cells/30 fish). **l**, Representative example of myelin sheaths in $mbpa^+$ oligodendrocytes eliminated by microglia. **m,n**, Immunohistochemistry (**m**) and quantification of anti-Mbp (cyan) inclusions (**n**) within microglia in animals carrying $Tg(mbpa:mCherry-CAAX)$ to label oligodendrocyte membrane. $n = 44$ mCherry-CAAX+ inclusions in 11 cells in 7 fish. All scale bars, 10 μm.

uncaging protocol elicited neuronal Ca^{2+} transients in sparsely labeled *neuroD*:GCaMP6s neurons most reliably within a 20-µm distance (Fig. 4i and Extended Data Fig. 4), consistent with previous findings[10]. We then used this measurement to determine the distance between

microglia and our uncaging target sites. We uncaged MNI-glutamate or DMSO control within 20 µm of microglia and performed timelapse imaging of process extension and retraction toward and away from the uncaging point (Fig. 4j and Supplementary Video 8). We found
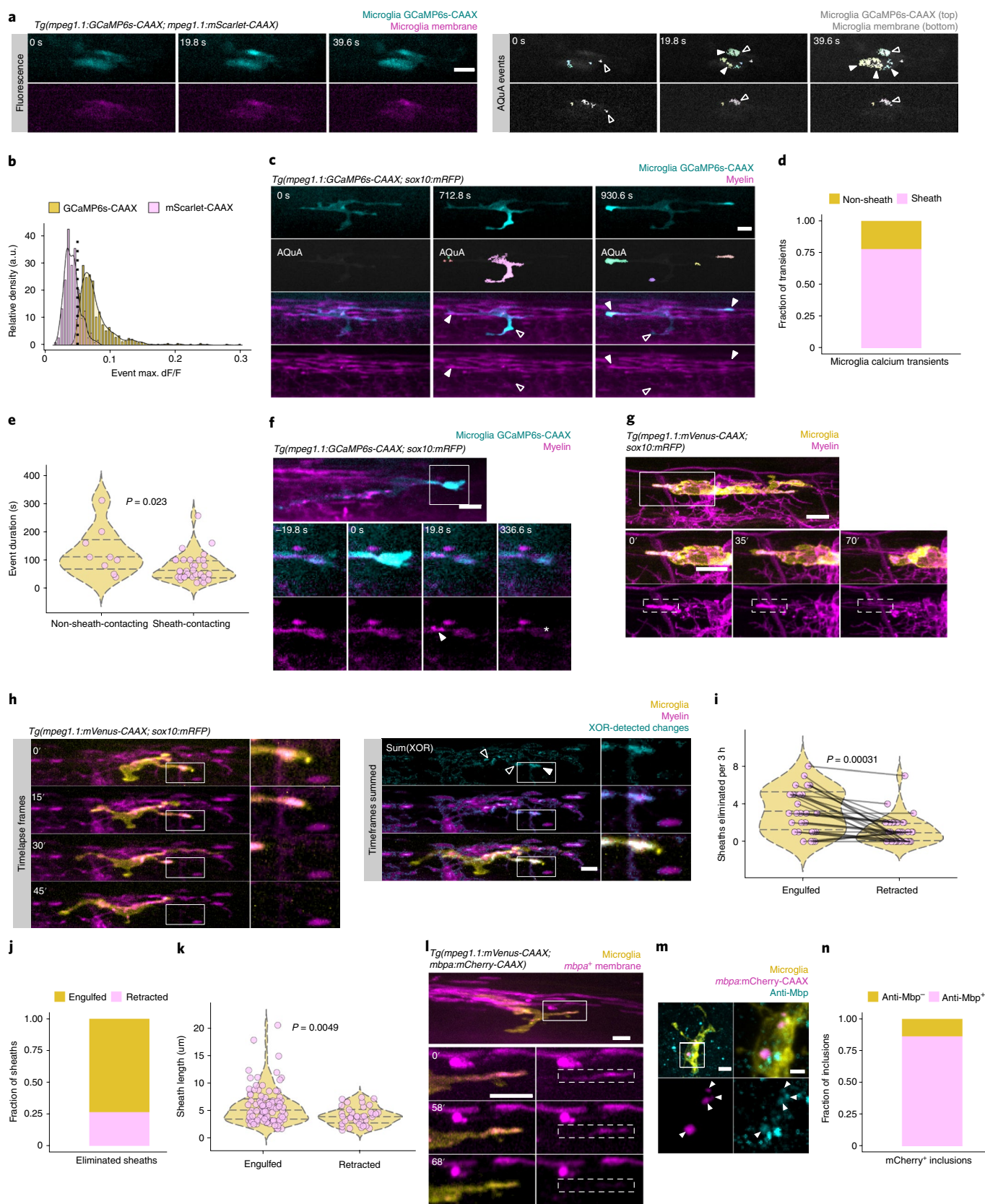
that microglia in both groups underwent the same number of processes movements (Fig. 4k), but glutamate uncaging caused microglia to elaborate processes in the direction of uncaging and to retract processes from the opposite side (see Methods) (Fig. 4l and Supplementary Video 8). Together, these data demonstrate that activity bidirectionally governs microglial interactions with neuronal somas.

If neuronal activity regulates microglial interaction with neuronal somas, could activity also reciprocally determine microglial phagocytosis of myelin from the tectal commissure? To test this possibility, we measured the amount of myelin phagocytosed by microglia following neuronal inhibition with dnVamp2 and BoNT/B (Fig. 5a). Similar to spinal cord, optic tectum microglia contained phagocytosed myelin (Fig. 5a). However, when neurons were silenced with either dnVamp2 or BoNT/B, optic tectum and spinal cord microglia contained many more myelin inclusions (Fig. 5b) and the total area of myelin inclusions per microglia was increased (Fig. 5c), despite no appreciable changes in either microglial area or the size of myelin inclusions (Fig. 5d,e). Together, these data indicate that microglia engulf more myelin from the tectal commissure when neuronal cell body layer activity is suppressed.

To test whether sustained increased activity in the cell body layer is sufficient to reduce myelin phagocytosis from the tectal commissure, we used a strong water current paradigm in which a magnetic stir bar generates strong water currents that force larvae to orient themselves and swim against the currents. Such visuomotor behaviors activate optic tectum[20], and this specific paradigm upregulated proteins associated with the optic tectum consistent with tectal activation[21]. We placed *Tg(mpeg1.1:mVenus-CAAX; mbpa:mCherry-CAAX)* larvae in strong water currents for 2 consecutive days, followed immediately by live imaging of myelin inclusions in tectal microglia (Fig. 5f,g). We found that exposure of larvae to strong water currents did not alter the morphology or size of tectal microglia (Fig. 5h), but microglia engulfed less myelin (Fig. 5i). Taken together with our observations that microglia engulfed more myelin following inhibition of cell body layer neurons (Fig. 5a–c), these data suggest that microglia phagocytose myelin in a bidirectional, neuronal activity-regulated manner.

Microglia regulate myelin targeting by oligodendrocytes. Microglia eliminate some, but not all, myelin sheaths (Fig. 2) and microglia phagocytose myelin in a neuronal activity-regulated manner (Fig. 5). Does microglial myelin phagocytosis refine myelin sheath number or targeting? To answer this, we eliminated microglia using three independent approaches and measured myelination by individual oligodendrocytes (Fig. 6a,b). First, we used an antisense morpholino oligonucleotide designed to block translation

of messenger RNA encoding interferon regulatory factor-8 (Irf8), which is required for macrophage specification and microglial development[22]. Second, we targeted Csf1r function, which is required for macrophage invasion of the CNS and microglial distribution[23], using a Csf1r inhibitor that has been used previously in larval zebrafish[24]. Because both of these methods eliminate microglia early in development and microglia support oligodendrocyte precursor cell (OPC) development[25,26], we took a third strategy to eliminate microglia specifically after myelination onset. We generated a transgenic line, *Tg(mpeg1.1:NTR-IRES-eGFP-CAAX)*, in which microglia express an enhanced variant of *Escherichia coli* nitroreductase ($NfsB^{T41Q/N71S/F124T}$) (NTR) to induce *mpeg1.1+* cell death upon treating larvae with the actuator, metronidazole. We quantified microglial ablation with each of these three strategies by adapting a neutral red assay previously used for quantifying microglia[23], and determined that they eliminate ~95, ~45 and ~75% of microglia, respectively (Fig. 6c,d).

To assess how microglia might refine myelin sheath formation, we examined the formation of myelin sheaths by individual oligodendrocytes in larvae in which microglia were eliminated using these approaches. To do so, we microinjected *Tol2.myrf:mScarlet-CAAX* DNA into one-cell-stage embryos to scatter-label oligodendrocytes via Tol2-mediated transgenesis (Fig. 6b). At 104 h post-fertilization (h.p.f.) we imaged oligodendrocytes in each of the eight groups (Fig. 6e and Extended Data Fig. 5a). We found that microglial depletion changed neither *mbpa+* oligodendrocyte number nor distribution (Extended Data Fig. 5b,c). However, tracing of myelin sheaths formed by individual oligodendrocytes revealed that, following microglial depletion (Irf8 MO, GW2580, NTR+/ metronidazole), oligodendrocytes had more sheaths than those in corresponding control groups (Fig. 6e,f) and these sheaths were also shorter in length (Fig. 6g). Furthermore, oligodendrocytes in the two severe depletion groups (Irf8 MO and NTR+/metronidazole) formed a number of spherical ensheathments, a phenomenon recently described as ectopic ensheathment of neuronal cell bodies[27] (Fig. 6h). These data indicate that microglial sheath pruning corrects myelin targeting and refines myelination by oligodendrocytes.

Discussion
Our work identifies microglia as mediators of myelin refinement by pruning of sheaths during development. Previous work established that microglial signaling to adhesion G protein-coupled receptors on OPCs promotes their differentiation, survival, and myelinogenesis[25,26]. Recently, single-cell RNA-sequencing analysis of rodent microglia detected *Mbp* mRNA, a myelin transcript that is enriched in myelin sheaths, within white matter microglia[28]. This finding

Fig. 3 | Microglia phagocytose myelin sheaths with minimal phagocytosis of oligodendrocyte somas. a, Strategy for delaying the breakdown of phagocytosed myelin with bafilomycin A1. **b**, Microglia in *Tg(mpeg1.1:mVenus-CAAX; mbpa:mCherry-CAAX)* larvae treated with DMSO or bafilomycin (1 μm) for 1 h before imaging. Arrowheads mark round myelin inclusions within microglia. **c**, Example sum-projected image of a microglia containing membrane RFP (mRFP) inclusions (top), with morphological segmentation performed using MorphoLibJ to identify inclusions (bottom). **d**, Histogram depicting the number of myelin inclusions per microglia in DMSO and bafilomycin-treated larva. **e–g**, Morphological segmentation on sum-projected images of microglia in 4 d.p.f. *Tg(mpeg1.1:mVenus-CAAX;mbpa:mCherry-CAAX)* larvae that were treated with either DMSO or bafilomycin before imaging. Each point represents one inclusion (**e**) or microglia (**f,g**); points are shaded so that overlapping points are visible (DMSO, n = 22 cells from 22 larvae containing 48 inclusions; bafilomycin, n = 22 cells from 22 larvae containing 175 inclusions). **e**, Area (μm²) of myelin inclusions within microglia, Wilcoxon rank-sum test. **f**, Total myelin inclusion area (μm²) per microglia, Wilcoxon rank-sum test. **g**, Number of myelin inclusions per microglia in bafilomycin-treated larvae over the course of developmental myelination (4–8 d.p.f.). Kruskal–Wallis test, n = fish/cells/inclusions, n = 10/10/74, 4 d.p.f.; 9/9/79, 5 d.p.f.; 12/12/101, 8 d.p.f. NS, not significant. **h**, Max-projection images of spinal cord oligodendrocytes (magenta) in larvae treated with either DMSO or bafilomycin A1 and live-stained with acridine orange (green). **i–k**, Quantification of *mbpa+* cells (**i**), acridine orange cells (**j**) and *mbpa+* cells stained by acridine orange (**k**) in 3.5 hemisegments and analyzed by Wilcoxon rank-sum test for n = fish/cells, n = 14/602 DMSO, 16/742 bafilomycin. **l**, Schematic of transgenic oligodendrocyte reporters that label either oligodendrocyte membrane (mCherry-CAAX) or cytosol (TagRFP). **m**, Examples of microglia in either *Tg(mpeg1.1:mVenus-CAAX;mbpa:mCherry-CAAX)* or *Tg(mpeg1.1:mVenus-CAAX; mbpa:TagRFP-T)* 4 d.p.f. larvae, treated with either DMSO or bafilomycin A1 before imaging. Arrowheads mark myelin inclusions. **n**, Number of mCherry-CAAX and TagRFP inclusions per microglia in each of the four groups presented in **m**, Wilcoxon rank-sum test (n = fish/cells/inclusions, n = 12/12/18 mCherry-CAAX + DMSO, 10/10/74 mCherry-CAAX + bafilomycin, 6/6/0 TagRFP + DMSO, 8/8/1 TagRFP + bafilomycin). Scale bars, 10 μm.

raised the possibility that microglia also engulf myelin under normal physiological conditions. By directly observing microglia–myelin interactions over development, we have discovered that microglia selectively phagocytose myelin sheaths to sculpt myelination.

What regulates the amount of myelin phagocytosed by microglia? We tested the possibility that neuronal activity regulates myelin engulfment, and found that microglial myelin phagocytosis is increased following neuronal silencing and decreased with activation (Fig. 5). This is reminiscent of previous studies showing that reducing neuronal activity limits myelin coverage of axons while increasing activity can bias axons for myelination and promote myelin growth[3,4]. Our work suggests that myelin plasticity is not confined to the axon–myelin unit but is additionally modifiable by other cell types, including microglia. How might microglia locate
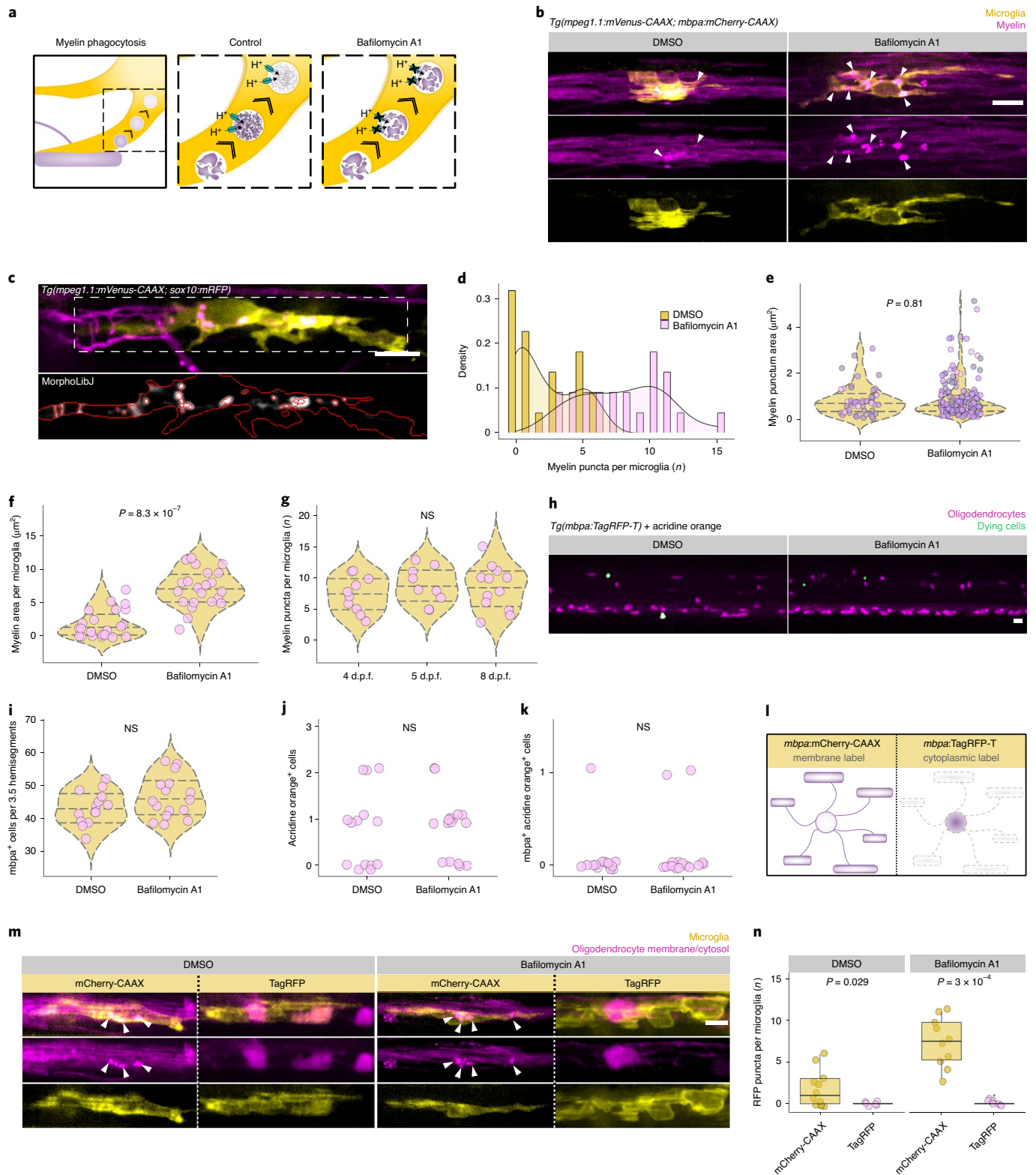
developing myelinated tracts? Volume transmission of extrasynaptic ATP from axons to oligodendrocyte lineage cells has been hypothesized to promote the myelination of white matter tracts[29]. In addition to signaling to oligodendrocyte lineage cells, ATP is sufficient to promote microglial translocation[30] and process extension in zebrafish optic tectum[10]. If such volume cues to OPCs are also sensed by microglia, ATP might regulate myelination by steering microglia toward or away from target neurons. Our work on the optic tectum suggested that the activity of one population of neurons, those in the periventricular cell body layer, dictated the microglial phagocytosis of myelin from a different population of axons, those in the tectal commissure (Fig. 5). This raises the intriguing possibility that the firing patterns of specific populations of neurons may regulate the myelination of nearby populations by directing microglial target interactions, perhaps contributing to the stereotyped myelination patterns of different axon tracts (Extended Data Fig. 6).

If microglia contribute to myelin plasticity, then brain regions with different densities of microglia, or different microglial states, might exhibit differences in myelin plasticity. During the larval stages we examined, microglia were present in the retina and optic tectum and, sparsely, in the spinal cord and forebrain, but were largely absent from other regions[23]. Recent work indicates that the myelination of at least one population of spinal cord neurons, the commissural primary ascending (CoPA) interneurons, is myelinated despite expression of tetanus neurotoxin to suppress activity[31]. CoPA axons project within the dorsal longitudinal fasciculus and are myelinated earlier than other neuron types[32]. One possibility for the insensitivity of CoPA myelination to silenced neuronal activity is that very few dorsal microglia are present at this stage (Fig. 1a,b), possibly preventing activity-regulated myelin phagocytosis. Somewhat conversely, treating mice with clinically relevant doses of methotrexate, a chemotherapeutic agent that induces persistent inflammatory microglia (CD68+, Iba1+), was sufficient to counteract activity-dependent myelin growth following optogenetic stimulation[3,33]. Together, these data support a role for microglial availability and state in regulating the dynamic range of activity-dependent myelination available to different brain regions.

Previously, the elimination of nascent myelin wraps was attributed to oligodendrocyte membrane resorption, a process referred to as 'retraction'[1,2,6,34]. Here we have shown that microglia also participate in myelin refinement by phagocytosing myelin sheaths (Fig. 2h–k). How do cell autonomous process retraction and microglial pruning work together to guide myelin patterning during development?

We have learned some properties of microglia–myelin interactions that may distinguish roles for each of these mechanisms. A larval zebrafish that has ~160 oligodendrocytes in the spinal cord may elaborate upwards of 2,400 nascent wraps before elimination. It is thus unlikely that the ~12 spinal cord microglia (Fig. 1b) are sufficiently numerous and motile to assess each nascent wrapping attempt. Indeed, extrapolating from our timelapse motility data, the average number of processes per microglia and number of microglia, we estimate that spinal microglia contact ~1,600 sheaths over a 24-h period. However, nearly all microglia we examined contained phagocytosed, Mbp+ myelin (Fig. 2m,n and Extended Data Fig. 2), and microglial depletion consistently increased sheath number and ectopic wrapping (Fig. 6). Additionally, the activity-regulated effects on myelin phagocytosis we describe here are similar to those reported on sheath retraction, with neuronal silencing increasing myelin elimination by both phagocytosis (Fig. 5) and nascent sheath retraction[1]. Together, these observations suggest that microglial myelin pruning complements autonomous retraction of newly forming myelin sheaths. Why might multiple mechanisms be necessary to eliminate nascent myelin? During wrapping, synthesized myelin is thought to spread over the axon surface like a liquid droplet[35], raising the possibility that oligodendrocyte processes that begin synthesizing myelin may not be easily retracted. Additionally, the formation of adhesive contacts between nascent sheaths and axons may preclude facile withdrawal[36,37], requiring pruning to disrupt attachment. Consistent with these possibilities, we found that sheaths engulfed by microglia were longer than those that were retracted (Fig. 2k). These observations raise the possibility that microglial myelin elimination extends the period of elimination after a developmental window for autonomous retraction has closed, perhaps due to the fluidity or adhesion of myelin.

What molecular cues might regulate phagocytosis? Mice deficient for multiple components of the classical branch of the complement cascade had extra synapses[38] and reduced synapse engulfment by microglia[12], raising the possibility that complement may also tag myelin sheaths for elimination. Consistent with this possibility, the outer lamellar myelin protein myelin oligodendrocyte glycoprotein binds the complement initiator C1q directly[39], myelin phagocytosis in vitro was augmented by complement[40] and multiple sclerosis lesions in postmortem brain tissue were immunoreactive for C3d, a cleavage product of complement component C3 (ref. [41]). However, just as recent work indicates that microglial synapse engulfment is complement independent in some brain

Fig. 4 | Neuronal activity regulates microglia–neuron interactions. a, (i) Coronal view of microglia and myelin in one hemisphere of optic tectum in a live Tg(mpeg1.1:mVenus-CAAX; mbpa:mCherry-CAAX) 5 d.p.f. larva. Dashed line marks the cell body layer, asterisks mark the neuropil layer, and arrowheads indicate the tectal commissure. (ii) Lateral view of microglia in the cell body layer. Microglia labeled by Tg(mpeg1.1:mScarlet-CAAX) and cell body layer glutamatergic neurons labeled by Tg(vglut2:eGFP). (i),(ii) Representative images from ten larvae. Scale bars, 50 μm. b, Top: max-projection images of optic tectum (lateral view) in Tg(mpeg1.1:mVenus-CAAX) larvae mosaically expressing neuroD:mTagBFP-CAAX or neuroD:mTagBFP-CAAX-2A-dnVamp2/BoNT/B (−2A-dnVamp2, −2A-BoNT/B). Bottom: single optical sections corresponding to a(i),(ii) containing microglial–neuron contacts (closed arrowheads) or absence of contact (open arrowheads). Asterisks mark neuropil. Scale bar, 50 μm. c, Fraction of neuron somas contacted per tectal field of view in each of the groups in b, analyzed by Wilcoxon rank-sum test with Bonferroni–Holm correction for multiple comparisons. d, Number of microglia per tectal field of view for each group in b, analyzed by Kruskal–Wallis test. b–d, n = fish/neurons/ microglia, n = 12/166/65 mTagBFP-CAAX, 15/487/66 mTagBFP-2A-dnVamp2, 22/398/121 mTagBFP-2A-BoNT/B. e, Max-projection images of microglia (yellow) and neurons sparsely expressing TRPV1-mTagBFP (cyan) in optic tectum of larvae treated with DMSO vehicle or 1 μm capsaicin. Closed arrowhead marks a microglia–neuron contact. Scale bar, 50 μm. f,g, Quantification of the fraction of TRPV1-mTagBFP+ neurons contacted by microglia (f) and the number of microglia per lateral tectum field of view (g). Each dot represents one larval tectum, analyzed by Wilcoxon rank-sum test (n = fish/neurons, n = 16/62 DMSO, 10/19 capsaicin). h, Schematic of glutamate uncaging and analysis of microglial motility. i, Example frames of glutamate uncaging near neurons sparsely labeled with GCaMP6s. Closed dot marks the point of uncaging, open dots show the position after uncaging and cell numbers match transient traces in a(ii). Representative example from one of nine larvae (Extended Fig. 4). Scale bar, 20 μm. j, Timelapse imaging frames of microglia in larvae treated with DMSO vehicle or MNI-glutamate, before and after focal 405-nm uncaging (at the open circle). Dotted lines divide microglia into uncaging and opposite sides (described in h) and arrowheads indicate newly formed processes. Scale bar, 10 μm. k,l, Total process extensions and retractions per cell in each group (k) and net movements toward the uncaging point (l). Wilcoxon rank-sum test, n = fish/microglia, n = 10/10 DMSO, 11/11 MNI-glutamate.

regions[42], studies of myelin phagocytosis have produced a number of complement-independent candidates that also appear to regulate myelin phagocytosis, including Fc-receptor gamma and scavenger receptor-AI/II[43]. Identifying the cues responsible for directing myelin removal, and the possibility that such a code may also be used by synapses, will probably inform strategies for treating myelin phagocytosis in disease.

Microglia are increasingly recognized for their roles in normal CNS development. Within the past two decades we have learned that microglia dynamically survey their environment in the absence of injury[44], in a manner that was recently unveiled to be directed by local noradrenergic tone[45,46]. Microglial interactions with both neurons and glia support development of the nervous system by eliminating structures and secreting trophic factors[12,47], influenced by and potentially contributing to regionalization of the brain[48]. Recently, a 10-month-old patient with a lethal mutation in CSF1R, a receptor required for microglial survival, was found to lack microglia and had epilepsy, agenesis of the corpus callosum and leukodystrophy, underscoring the important and numerous roles played by microglia in development of the nervous system[49]. By revealing that microglia tune CNS myelination, our study now raises the possibility that interactions among microglia, neurons, and oligodendrocytes contribute to the development of brain function.
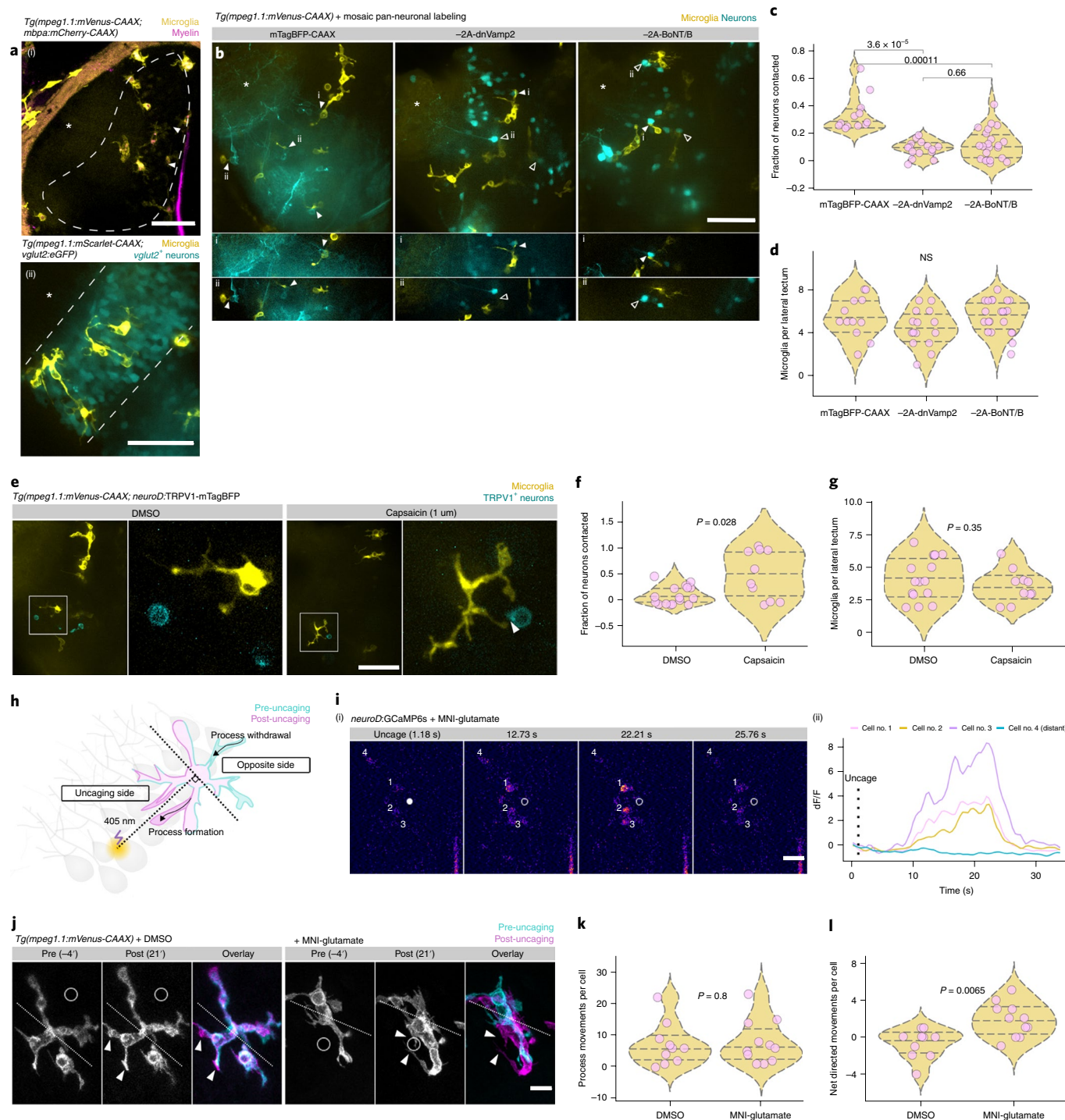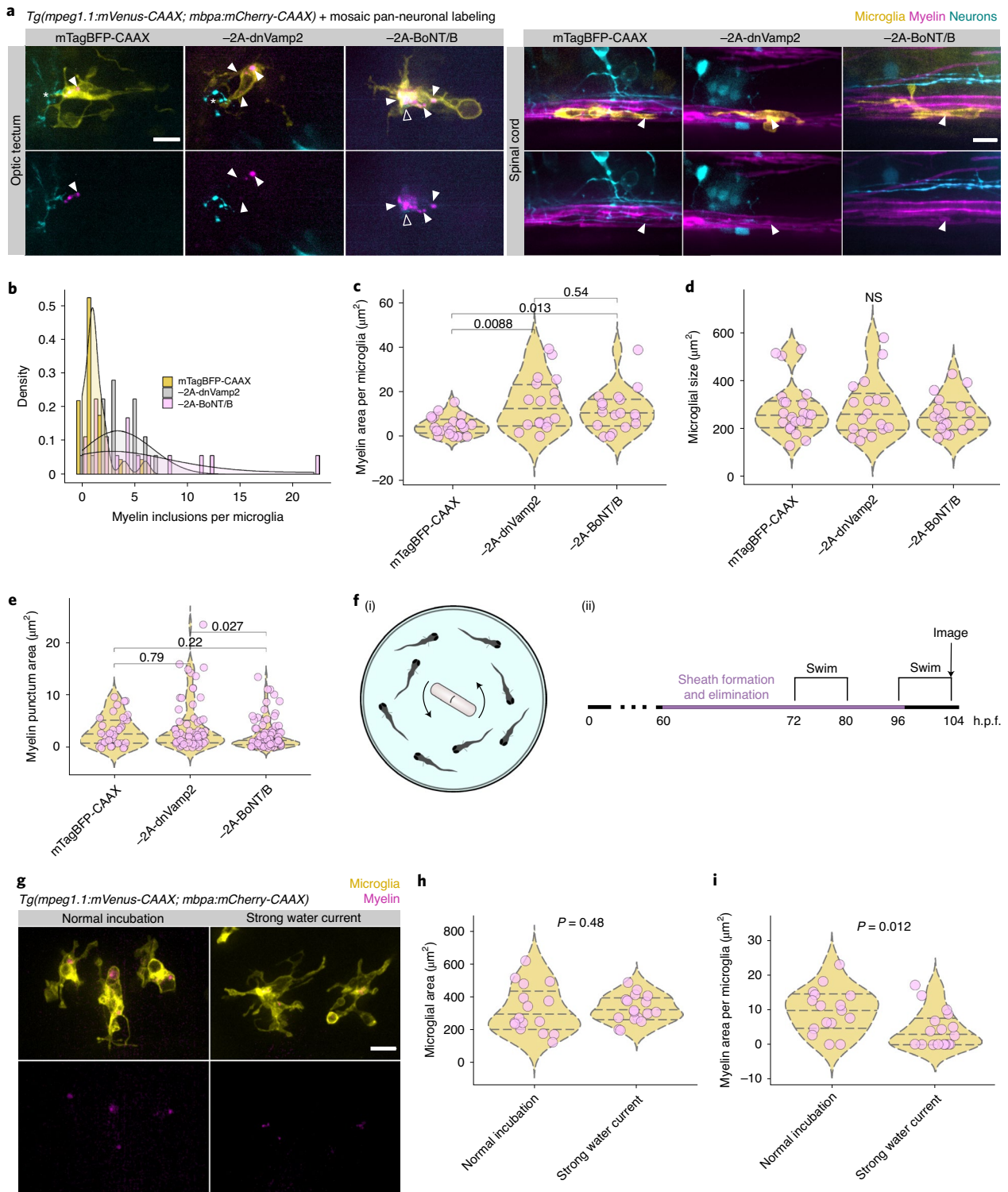
Fig. 5 | Neuronal activity regulates myelin phagocytosis by microglia. a, Microglia in the optic tectum and spinal cord in larvae carrying *Tg(mpeg1.1:mVenus-CAAX; mbpa:mCherry-CAAX)* to label microglia and myelin and mosaically expressing either *neuroD*:mTagBFP-CAAX or *neuroD*:mTagBFP-CAAX-2A-dnVamp2/BoNT/B (−2A-dnVamp2, −2A-BoNT/B). Closed arrowheads mark myelin inclusions within microglia (magenta); open arrowheads mark neuronal inclusions (cyan); asterisks mark microglial processes contacting neurons. Scale bars, 10 μm. **b–e**, MorphoLibJ morphological segmentation on sum-projected images of optic tectum microglia at 4 d.p.f. in each group in **a**. Each point represents one microglia (**c**,**d**) or inclusion (**e**) (*n*=fish/microglia/inclusions, *n*=18/23/30 mTagBFP-CAAX, 18/18/63 mTagBFP-2A-dnVamp2, 18/18/87 mTagBFP-2A-BoNT/B). **b**, Histogram depicting the number of myelin inclusions within microglia. **c**, Total myelin inclusion area per microglia, Wilcoxon rank-sum test with Bonferroni–Holm correction for multiple comparisons. **d**, Microglia area, Kruskal–Wallis test. **e**, Area of individual myelin inclusions within microglia, Wilcoxon rank-sum test. **f**, Schematic and timeline of strong water current-induced forced swimming to increase neuronal activity in optic tectum. **g**, Representative examples of microglia containing myelin inclusions in normal incubation and forced swim paradigms. Scale bar, 10 μm. **h**,**i**, Microglial area (**h**) and myelin inclusion area (**i**) per cell in each group, Wilcoxon rank-sum test (*n*=fish/microglia, *n*=12/16 normal, 13/17 strong currents).
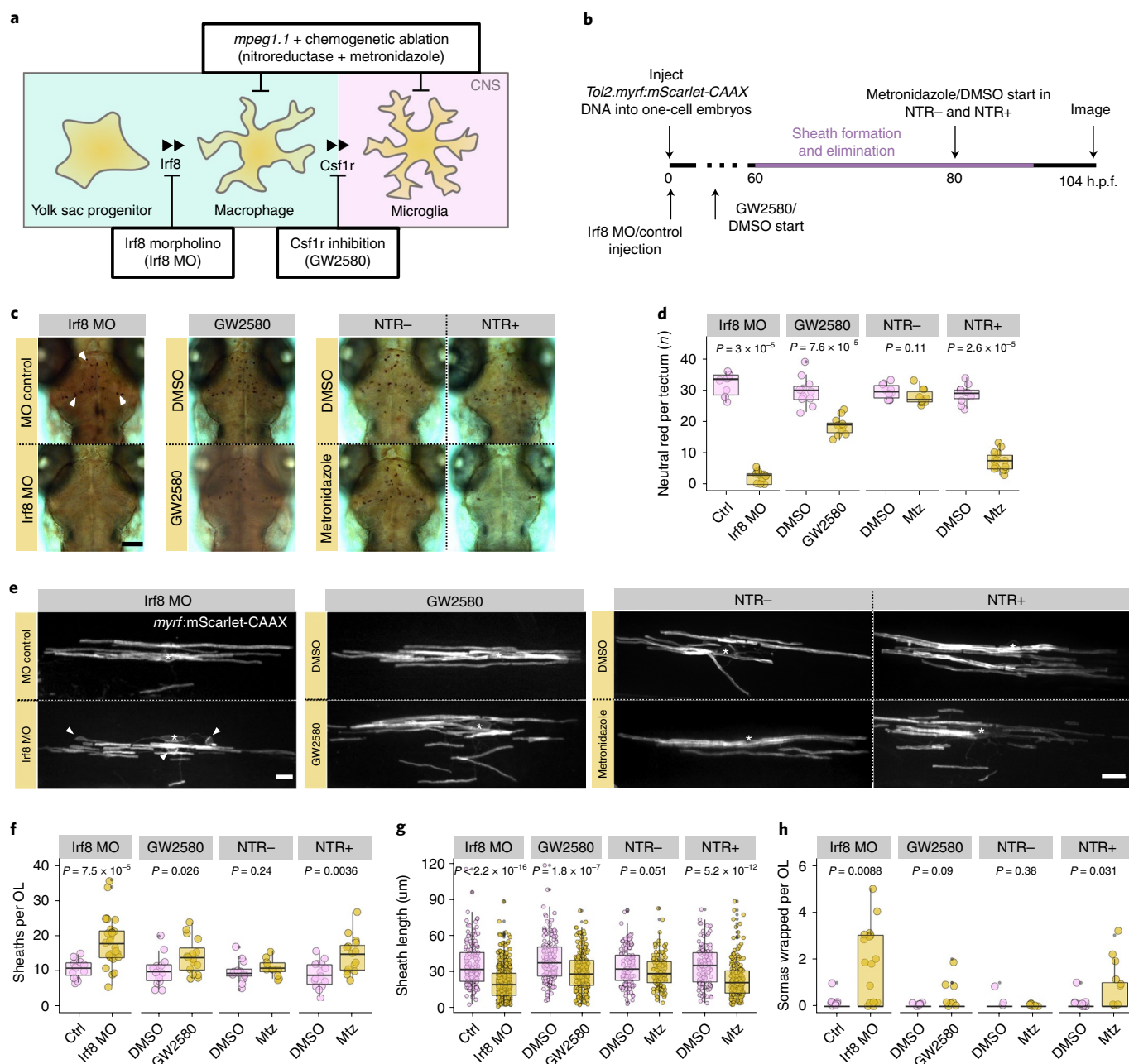
Fig. 6 | Microglial ablation during myelination increases myelin sheath number. a, Schematic of microglial development and three approaches to ablation of microglia. **b**, Timeline for labeling of individual oligodendrocytes by microinjection at the one-cell stage and ablation of microglia either by coinjection with Irf8 translation-blocking MO, treatment with Csf1r inhibitor GW2580 or NTR treatment with metronidazole. **c**, Brightfield images of live neutral red-stained larvae in each of three ablation groups. Arrowheads mark examples of neutral red-labeled microglia in optic tectum (small red dots). Scale bar, 100 μm. **d**, Quantification of neutral red-labeled microglia in the optic tectum of larvae in each group. Each dot represents the microglial count in one larva. Wilcoxon rank-sum test, left to right, n = fish/microglia, n = 10/319, 15/35, 12/357, 11/206, 10/296, 10/279, 10/288, 16/120. **e**, Example spinal cord oligodendrocytes labeled by *myrf*:mScarlet-CAAX in each group. Asterisks mark oligodendrocyte (OL) somas, and arrowheads indicate myelinated cell bodies. Scale bar, 10 μm. **f–h**, Quantification of sheath number (**f**), length (**g**) and ectopic soma wraps (**h**; example in **e**) in each group. Each point represents one oligodendrocyte (**f**), sheath (**g**) or soma wrap (**h**). Wilcoxon rank-sum test, left to right, n = cells/fish/sheaths, n = 15/15/163, 27/27/503, 15/15/156, 16/16/229, 12/12/121, 11/11/124, 15/15/139, 15/15/223. Scale bars, 10 μm.

Online content

Any methods, additional references, Nature Research reporting summaries, source data, extended data, supplementary information, acknowledgements, peer review information; details of author contributions and competing interests; and statements of data and code availability are available at https://doi.org/10.1038/s41593-020-0654-2.

References

1. Hines, J. H., Ravanelli, A. M., Schwindt, R., Scott, E. K. & Appel, B. Neuronal activity biases axon selection for myelination in vivo. *Nat. Neurosci.* **18**, 683–689 (2015).

2. Mensch, S. et al. Synaptic vesicle release regulates myelin sheath number of individual oligodendrocytes in vivo. *Nat. Neurosci.* **18**, 628–630 (2015).

3. Gibson, E. M. et al. Neuronal activity promotes oligodendrogenesis and adaptive myelination in the mammalian brain. *Science* **344**, 1252304 (2014).

4. Mitew, S. et al. Pharmacogenetic stimulation of neuronal activity increases myelination in an axon-specific manner. *Nat. Commun.* **9**, 306 (2018).

5. Scholz, J., Klein, M. C., Behrens, T. E. J. & Johansen-Berg, H. Training induces changes in white-matter architecture. *Nat. Neurosci.* **12**, 1370–1371 (2009).

6. Hughes, E. G., Orthmann-Murphy, J. L., Langseth, A. J. & Bergles, D. E. Myelin remodeling through experience-dependent oligodendrogenesis in the adult somatosensory cortex. *Nat. Neurosci.* **21**, 696–706 (2018).

7. Sampaio-Baptista, C. et al. Motor skill learning induces changes in white matter microstructure and myelination. *J. Neurosci.* **33**, 19499–19503 (2013).

8. McKenzie, I. A. et al. Motor skill learning requires active central myelination. *Science* **346**, 318–322 (2014).

9. Liu, P., Du, J. & He, C. Developmental pruning of early-stage myelin segments during CNS myelination in vivo. *Cell Res.* **23**, 962–964 (2013).

10. Li, Y., Du, X., Liu, C., Wen, Z.-L. & Du, J. Reciprocal regulation between resting microglial dynamics and neuronal activity in vivo. *Dev. Cell* **23**, 1189–1202 (2012).

11. Tremblay, M.-È., Lowery, R. L. & Majewska, A. K. Microglial interactions with synapses are modulated by visual experience. *PLoS Biol.* **8**, e1000527 (2010).

12. Schafer, D. P. et al. Microglia sculpt postnatal neural circuits in an activity and complement-dependent manner. *Neuron* **74**, 691–705 (2012).

13. Hong, S. et al. Complement and microglia mediate early synapse loss in Alzheimer mouse models. *Science* **352**, 712–716 (2016).

14. Neumann, H., Kotter, M. R. & Franklin, R. J. M. Debris clearance by microglia: an essential link between degeneration and regeneration. *Brain* **132**, 288–295 (2009).

15. Uranova, N. A., Vikhreva, O. V., Rachmanova, V. I. & Orlovskaya, D. D. Ultrastructural alterations of myelinated fibers and oligodendrocytes in the prefrontal cortex in schizophrenia: a postmortem morphometric study. *Schizophr. Res. Treatment* **2011**, 325789 (2011).

16. Pozner, A. et al. Intracellular calcium dynamics in cortical microglia responding to focal laser injury in the PC::G5-tdT reporter mouse. *Front. Mol. Neurosci.* **8**, 12 (2015).

17. Eichhoff, G., Brawek, B. & Garaschuk, O. Microglial calcium signal acts as a rapid sensor of single neuron damage in vivo. *Biochim. Biophys. Acta Mol. Cell Res.* **1813**, 1014–1024 (2011).

18. Sieger, D., Moritz, C., Ziegenhals, T., Prykhozhij, S. & Peri, F. Long-range Ca²⁺ waves transmit brain-damage signals to microglia. *Dev. Cell* **22**, 1138–1148 (2012).

19. Bai, Q., Sun, M., Stolz, D. B. & Burton, E. A. Major isoform of zebrafish P0 is a 23.5 kDa myelin glycoprotein expressed in selected white matter tracts of the central nervous system. *J. Comp. Neurol.* **519**, 1580–1596 (2011).

20. Nevin, L. M., Robles, E., Baier, H. & Scott, E. K. Focusing on optic tectum circuitry through the lens of genetics. *BMC Biol.* **8**, 126 (2010).

21. Langebeck-Jensen, K., Shahar, O. D., Schuman, E. M., Langer, J. D. & Ryu, S. Larval zebrafish proteome regulation in response to an environmental challenge. *Proteomics* https://doi.org/10.1002/pmic.201900028 (2019).

22. Shiau, C. E., Kaufman, Z., Meireles, A. M. & Talbot, W. S. Differential requirement for irf8 in formation of embryonic and adult macrophages in zebrafish. *PLoS ONE* **10**, e0117513 (2015).

23. Herbomel, P., Thisse, B. & Thisse, C. Zebrafish early macrophages colonize cephalic mesenchyme and developing brain, retina, and epidermis through a M-CSF receptor-dependent invasive process. *Dev. Biol.* **238**, 274–288 (2001).

24. Green, L. A., Nebiolo, J. C. & Smith, C. J. Microglia exit the CNS in spinal root avulsion. *PLoS Biol.* **17**, e3000159 (2019).

25. Wlodarczyk, A. et al. A novel microglial subset plays a key role in myelinogenesis in developing brain. *EMBO J.* **36**, 3292–3308 (2017).

26. Giera, S. et al. Microglial transglutaminase-2 drives myelination and myelin repair via GPR56/ADGRG1 in oligodendrocyte precursor cells. *eLife* **7**, e33385 (2018).

27. Almeida, R. G. et al. Myelination of neuronal cell bodies when myelin supply exceeds axonal demand. *Curr. Biol.* **28**, 1296–1305 (2018).

28. Li, Q. et al. Developmental heterogeneity of microglia and brain myeloid cells revealed by deep single-cell RNA sequencing. *Neuron* **101**, 207–223 (2019).

29. Fields, R. D. Volume transmission in activity-dependent regulation of myelinating glia. *Neurochem. Int.* **45**, 503–509 (2004).

30. Davalos, D. et al. ATP mediates rapid microglial response to local brain injury in vivo. *Nat. Neurosci.* **8**, 752–758 (2005).

31. Koudelka, S. et al. Individual neuronal subtypes exhibit diversity in CNS myelination mediated by synaptic vesicle release. *Curr. Biol.* https://doi.org/10.1016/j.cub.2016.03.070 (2016).

32. Nelson, H. N. et al. Individual neuronal subtypes control initial myelin sheath growth and stabilization. Preprint at *bioRxiv* https://doi.org/10.1101/809996 (2019).

33. Geraghty, A. C. et al. Loss of adaptive myelination contributes to methotrexate chemotherapy-related cognitive impairment. *Neuron* **193**, 250–265 (2019).

34. Baraban, M., Koudelka, S. & Lyons, D. A. Ca²⁺ activity signatures of myelin sheath formation and growth in vivo. *Nat. Neurosci.* **21**, 19–23 (2018).

35. Nawaz, S. et al. Actin filament turnover drives leading edge growth during myelin sheath formation in the central nervous system. *Dev. Cell* **34**, 139–151 (2015).

36. Elazar, N. et al. Axoglial adhesion by Cadm4 regulates CNS myelination. *Neuron* **101**, 224–231 (2018).

37. Hughes, A. N. & Appel, B. Oligodendrocytes express synaptic proteins that modulate myelin sheath formation. *Nat. Commun.* **10**, 4125 (2019).

38. Stevens, B. et al. The classical complement cascade mediates CNS synapse elimination. *Cell* **131**, 1164–1178 (2007).

39. Brunner, C., Lassmann, H., Waehneldt, T. V., Matthieu, J. M. & Linington, C. Differential ultrastructural localization of myelin basic protein, myelin/ oligodendroglial glycoprotein, and 2′,3′-cyclic nucleotide 3′-phosphodiesterase in the CNS of adult rats. *J. Neurochem.* **52**, 296–304 (1989).

40. van der Laan, L. J. et al. Macrophage phagocytosis of myelin in vitro determined by flow cytometry: phagocytosis is mediated by CR3 and induces production of tumor necrosis factor-alpha and nitric oxide. *J. Neuroimmunol.* **70**, 145–152 (1996).

41. Barnett, M. H., Parratt, J. D. E., Cho, E. S. & Prineas, J. W. Immunoglobulins and complement in postmortem multiple sclerosis tissue. *Ann. Neurol.* **65**, 32–46 (2009).

42. Gunner, G. et al. Sensory lesioning induces microglial synapse elimination via ADAM10 and fractalkine signaling. *Nat. Neurosci.* **22**, 1075–1088 (2019).

43. Rotshenker, S. et al. Galectin-3/MAC-2, ras and PI3K activate complement receptor-3 and scavenger receptor-AI/II mediated myelin phagocytosis in microglia. *Glia* **56**, 1607–1613 (2008).

44. Nimmerjahn, A., Kirchhoff, F. & Helmchen, F. Resting microglial cells are highly dynamic surveillants of brain parenchyma in vivo. *Science* **308**, 1314–1318 (2005).

45. Stowell, R. D. et al. Noradrenergic signaling in the wakeful state inhibits microglial surveillance and synaptic plasticity in the mouse visual cortex. *Nat. Neurosci.* **22**, 1782–1792 (2019).

46. Liu, Y. U. et al. Neuronal network activity controls microglial process surveillance in awake mice via norepinephrine signaling. *Nat. Neurosci.* **22**, 1771–1781 (2019).

47. Brown, G. C. & Neher, J. J. Microglial phagocytosis of live neurons. *Nat. Rev. Neurosci.* **15**, 209–216 (2014).

48. De Biase, L. M. et al. Local cues establish and maintain region-specific phenotypes of basal ganglia microglia. *Neuron* **95**, 341–356 (2017).

49. Oosterhof, N. et al. Homozygous mutations in CSF1R cause a pediatric-onset leukoencephalopathy and can result in congenital absence of microglia. *Am. J. Hum. Genet.* **104**, 936–947 (2019).

Methods

Zebrafish lines and husbandry. All animal work was approved by the Institutional Animal Care and Use Committee at the University of Colorado School of Medicine. Zebrafish embryos were raised at 28.5 °C in embryo medium and staged according to hours or days postfertilization (h.p.f./d.p.f.) and morphological criteria[50].

We used the previously established transgenic lines *Tg(sox10:mRFP)*[vu234], *Tg(mbpa:tagRFP)*[co25], *Tg(vglut2:eGFP)*[51] and *Tg(mbpa:mCherry-CAAX)*[co13].

We also generated and used the new lines *Tg(mpeg1.1:mVenus-CAAX)*[co56], *Tg(mpeg1.1:NTR-IRES-eGFP-CAAX)*[co57], *Tg(mpeg1.1:mScarlet-CAAX)*[co62] and *Tg(mpeg1.1:GCaMP6s-CAAX)*[co65]. All other reporters were expressed by transient transgenesis to achieve sparse labeling.

Plasmid construction and generation of transgenic zebrafish. Tol2 expression plasmids were generated by Multisite Gateway cloning and injected into one-cell embryos with Tol2 mRNA to generate transient transgenic animals. The following entry clones[52] were used in LR recombination reactions to generate expression plasmids:

p5E-neuroD, *p5E-myrf*, *p5E-mpeg1.1* (ref. [53])

pME-NTR (*NfsB*[T41Q/N71S/F124T])[54], *pME-mTagBFP-CAAX* no stop, *pME-mTagBFP-CAAX* with stop, *pME-mVenus-CAAX*, *pME-mScarlet-CAAX*, *pME-GCaMP6s-CAAX*[37] and *pME-GCaMP6s*, *pME-TRPV1* (*R. norvegicus*)[55]

p3E-polyA, *p3E-2A-dnVamp2* (ref. [37]), *p3E-2A-BoNT/B*[37], *p3E-IRES-eGFP-CAAX* and *p3E-mTagBFP*

pDEST-Tol2-pA, *pDEST-Tol2-CG2* (green heart marker) and *pDEST-Tol2-CR2* (red heart marker)

To generate *pME-GCaMP6s* and *pME-TRPV1* we PCR amplified attB1-attB2-flanked coding sequences of GCaMP6s and TRPV1 using templates *pGP-CMV-GCaMP6s* (Addgene, no. 40753) and *UAS:TRPV1-TagRFP*[55] and the following primers:

attB1-GCaMP6s:
GGGGACAAGTTTGTACAAAAAAGCAGGCTACCATGGGTTCTCA
TCATCATCA

attB2-GCaMP6s:
GGGGACCACTTTGTACAAGAAAGCTGGGTTCTTCGCTGTCATCA
TTTGTACA

attB1-TRPV1:
GGGGACAAGTTTGTACAAAAAAGCAGGCTACCATGGAACAACGGGC
TAGCTTA

attB2-TRPV1:
GGGGACCACTTTGTACAAGAAAGCTGGGTTTTTCTCCCCTGGGACC
ATGG

attB1-attB2-flanked amplicons were gel purified, recombined with pDONR-221 to generate pMEs, Sanger sequenced and then LR-recombined with entry vectors to generate Tol2 expression plasmids *neuroD:GCaMP6s-pA-CR2* and *neuroD:TRPV1-mTagBFP-pA-CR2*.

Drug treatments. Bafilomycin A1 (Tocris, cat. no. 1334) was diluted in DMSO and larvae were treated with 1 µM in embryo medium for 1 h at 28.5 °C before mounting in agarose for live imaging. An equivalent volume of DMSO (0.1%) was used as vehicle control.

Metronidazole (Sigma, no. M1547) was diluted to 10 mM in 0.1% DMSO in embryo medium immediately before use for nitroreductase-mediated cell ablation[54]. Metronidazole is light sensitive, so all four treatment groups were kept in the incubator in the dark starting at administration (80 h.p.f.).

Neutral red (Sigma, no. N7005) was diluted to 2.5 µg ml⁻¹ in embryo medium and administered to 4 d.p.f. larvae and raised in 0.003% PTU (Sigma, no. P7629) to prevent pigmentation for 2.5 h at 28.5 °C in the dark[23,56]. Following staining, larvae were washed two or three times in fresh media and monitored until nonspecific tissue redness had washed out (30–60 min), before mounting dorsal-down in low-melt agarose for widefield, brightfield imaging (×10) of optic tectum microglia.

GW2580 (ApexBio, no. A1655) was diluted in DMSO and administered at 100 µm in embryo medium to 48-h.p.f. larvae with drug refresh every 24 h. An equivalent volume of DMSO (0.2%) was used as vehicle control.

Capsaicin (Sigma, no. M2028) was diluted in DMSO and administered at 1 µm in embryo medium 2 h before imaging. An equivalent volume of DMSO (0.1%) was used as vehicle control.

MNI-glutamate (Tocris, cat. no. 1490) was diluted in DMSO to 50 mM and administered at 1 µm in embryo medium 1 h before imaging. An equivalent volume of DMSO (0.02%) was used as vehicle control. After 1 h, a small incision was made in larval tails to assist pancuronium bromide neuromuscular junction paralysis for timelapse imaging (see Imaging and image analysis). Larvae were kept in the dark as much as possible during treatment, paralysis and agarose mounting. MNI-glutamate and DMSO were focally uncaged with a 405-nm laser applied to a circular region of interest (ROI) (~2.5-µm radius) in the center of the acquired z-stack (microglia) or in the same plane of imaging (neurons).

Acridine orange (Sigma, no. A6014) was diluted in embryo medium to 3 µg ml⁻¹ and larvae were treated for 30 min, washed twice and immediately live imaged[57].

Strong water currents/forced swim paradigm. Larvae were placed in 30-mm dishes with or without a stir bar and maintained at 28.5 °C on a stir plate at 350 r.p.m. for 8 h per day for 2 consecutive days, at 3 and 4 d.p.f. (ref. [21]), followed immediately by live imaging of myelin inclusions in tectal microglia.

Morpholino injection. A published translation-blocking antisense morpholino oligodendrocyte directed against *Irf8* (ref. [58]) (GeneTools) (TCAGTCTGCGACCGCCCGAGTTCAT) was diluted to 2 mM in water and used to prepare a 1.5 ng nl⁻¹ injection solution that also contained Tol2 mRNA and *Tol2. myrf:mScarlet-CAAX* DNA for oligodendrocyte labeling. Injection solution (3 nl) was injected into the yolk of one-cell-stage embryos. Control injection solution was similar, except that morpholino was replaced with an equivalent volume of water.

Immunohistochemistry. At 6 d.p.f., *Tg(mpeg1.1:mVenus-CAAX; mbpa:mCherry-CAAX)* larvae were fixed at 4 °C overnight in 4% paraformaldehyde/1× PBS. Larvae were washed in PBS and embedded in 1.5% agar/30% sucrose blocks placed in 30% sucrose overnight at 4 °C. Blocks were frozen in 2-methyl butane chilled by immersion in liquid nitrogen. Sections (20 µm) were cut and collected on microscope slides then rehydrated with PBS, washed with PBS containing 0.1% Triton X-100 (PBSTx) and blocked with 2% goat serum/2% bovine serum albumin in PBSTx for 1 h at room temperature. Rabbit anti-Mbpa antibody[59] was applied at 1:200 dilution in blocking solution overnight at 4 °C. The sections were washed with PBSTx and then incubated with Alexa Fluor 647 goat anti-rabbit antibody (Jackson ImmunoResearch, no. 111–606–044) at 1:200 dilution in blocking solution for 2 h at room temperature. Slides were washed again with PBSTx, covered with Vectashield, and coverslipped.

Statistics and reproducibility. All statistics were performed in R (v.3.4.1) with RStudio. Plots were generated using dplyr and ggplot2 packages with cowplot package formatting, and all statistical tests were performed using ggpubr functions. We used the two-tailed Wilcoxon rank-sum test (Mann–Whitney), with no assumption of normality, for all unpaired comparisons. For multiple comparisons, we first assessed global significance using the Kruskal–Wallis test, followed by pairwise Wilcoxon rank-sum tests with Bonferroni–Holm correction for multiple comparisons. Violin plots and box plots show quantiles (25, 50 and 75%) with the central line marking the median. Violin plot colors are not meaningful, and only the axes specify the groups. For other plot types, including stacked bar plots and histograms, legends are provided to explain grouping colors. We considered $P < 0.05$ the threshold for statistical significance, and provided exact P values; $P > 0.05$ is listed as not significant. All representative images shown are derived from the datasets analyzed, so the number (n) of biological replicates is the number of times each imaging experiment was performed. Embryos and larvae were randomly allocated to groups. All image analysis was performed blind using the Fiji plugin Lab-utility-plugins/blind-files. Image acquisition was not blinded, but identical anatomical regions were imaged in all larvae.

Imaging and image analysis. We performed live imaging on larvae embedded in 1.2% low-melt agarose containing either 0.02% tricaine or 0.3 mg ml⁻¹ pancuronium bromide (Sigma, no. P1918) for immobilization. We acquired images using a Plan Apochromat ×20/0.8 numerical aperture (NA) (with ×1.6 optivar) air, and C-Apochromat ×40/1.1 NA water- and ×63/1.2 NA water-immersion objectives on a Zeiss LSM 880 and a Zeiss CellObserver Spinning Disk confocal system equipped with a Photometrics Prime 95B camera. We collected images of neutral red-stained larvae using a Zeiss AxioObserver microscope. After collection of images with Zen (Carl Zeiss), we performed all processing and analysis using Fiji/ImageJ.

Neuronal calcium imaging. Embryos were injected at the one-cell stage with Tol2 mRNA and *Tol2.neuroD:GCaMP6s*. Mosaically labeled neurons in the hindbrain and midbrain were imaged at ~4 Hz for 50 s following uncaging of MNI-glutamate or DMSO. Identifiable cell bodies were traced in Fiji, along with a background ROI, and mean fluorescence intensity values for each cell at each time point were background-subtracted and divided by the average fluorescence intensity of frames before uncaging (baseline) to generate dF/F values. We considered dF/F events >0.5 as transients, which generally correlated with visible changes in GCaMP6s fluorescence. The distance of each cell centroid to the uncaging point was measured by linear ROI to determine the distance of cells versus the likelihood of exhibiting a transient in response to uncaging.

Microglia calcium imaging. Larvae (4 d.p.f.) were timelapse imaged using a ×20 air objective with ×1.6 optivar. Z-stacks of five slices with Nyquist (oversampled) spacing were acquired every 5–20 s for 10–20 min. Single-channel images were processed in AQuA[60] (Fiji) with the parameters listed in Supplementary Table 3. For mScarlet-CAAX events, all events were used for analysis. Following determination that, for most of these membrane 'events', dF/F<0.05, we filtered GCaMP6s-CAAX events such that dF/F > 0.05. A smaller filtered dataset containing only events with dF/F > 0.10 and area > 3 µm² was generated in R and used to assess sheath-contacting and non-contacting process transients.

Sheath engulfment versus retraction analysis. *Tg(mpeg1.1:mVenus-CAAX; sox10:mRFP)* 4 d.p.f. larvae were timelapse imaged using a ×20 air objective with ×1.6 optivar (spinning disk details). Z-stacks of uniform (Nyquist) slice number and spacing were acquired in the spinal cord every 10–15 min for 3 h. At each time point, slices were sum projected to preserve all signal for intensity-based analysis. Then, frames were registered to correct for drift and corrected for photobleaching using the exponential fit method. To identify myelin changes over time in an automated and unbiased way, the myelin channel was then subjected to a custom-written progressive XOR processing scheme (Supplementary Table 2) in which the Image Calculator performs the XOR operation on consecutive timelapse frames and generates a new series of frames containing only signal present in frame i or frame $i+1$ but not both, therefore including signal from only the myelin transgene that changes over time in the original timelapse. This progressive XOR series was then sum projected to generate an output image containing all changes in the myelin transgene signal over time. Merging with the original timelapse, projected into a single frame, marked sheaths that had disappeared (or appeared) during the timelapse acquisition. We then examined the fate of these XOR-identified sheaths in the original timelapse. Sheaths that appeared or disappeared were examined for microglial contact in the original timelapse, while those that appeared to be engulfed and were marked by our XOR series were counted as phagocytosed. Noncontacted sheaths that disappeared were counted as retracted.

Microglia process motility analysis. Larvae were immobilized by immersion in pancuronium bromide (Sigma, no. P1918) at 0.3 mg ml^{-1}, aided by a small incision at the tip of the tail, before mounting in agarose. Timelapse z-stack frames were acquired every 2.5 min for 1 h. Movies were max-projected at every time frame, registered to correct for drift and cells were manually tracked from frame to frame for process maintenance, withdrawal or formation of new processes. Events occurring at distalmost (usually primary or secondary) processes were tracked. In response to glutamate uncaging, two values were calculated: total process movements and net directed process movements. Total process movements = uncaging new + uncaging lost + opposite new + opposite lost, and net directed process movements = (uncaging new + opposite lost) – (uncaging lost + opposite new), where the uncaging side is the side of the microglia facing (orthogonal to) the uncaging site, and the opposite side is the side of the microglia facing away.

Myelin inclusion measurements. Z-stack images of microglia, acquired with uniform optical sectioning and number of slices, were sum projected in Fiji. The microglial border was manually traced and the background cleared. The channels were split and the myelin channel was subjected to morphological segmentation using the Fiji plugin MorphoLibJ[61]. Specific parameters were: object image, gradient Type = morphological, gradient radius = 1 px, watershed segmentation tolerance = 60 (spinal cord) or 20 (optic tectum). Watershed segmentation values were predetermined on sample images of microglia from both regions. Following segmentation, the wand tool was used to trace watershed ROIs, and ROI and total cell area values were saved for downstream analysis in R.

Sheath length measurement. Z-stack images of oligodendrocytes, acquired with uniform optical sectioning, were traced in 3D using the Fiji plugin Simple Neurite Tracer[62]. The number of paths (sheaths) belonging to a single oligodendrocyte is the number of sheaths per cell, and the path length in 3D is the sheath length. Default parameters were used, except cursor snapping = 2 XY pixels. Path lengths were exported to R for analysis.

Reporting Summary. Further information on research design is available in the Nature Research Reporting Summary linked to this article.

Data, code and materials availability
All data are available in the manuscript, the Source Data files or the Supplementary Information. Fiji scripts are available in the Supplementary Information. All plasmids and transgenic zebrafish are available by request.

References

50. Kimmel, C. B., Ballard, W. W., Kimmel, S. R., Ullmann, B. & Schilling, T. F. Stages of embryonic development of the zebrafish. *Dev. Dyn.* **203**, 253–310 (1995).
51. Higashijima, S.-I., Mandel, G. & Fetcho, J. R. Distribution of prospective glutamatergic, glycinergic, and GABAergic neurons in embryonic and larval zebrafish. *J. Comp. Neurol.* **480**, 1–18 (2004).
52. Kwan, K. M. et al. The Tol2kit: a multisite gateway-based construction Kit for Tol2 transposon transgenesis constructs. *Dev. Dyn.* **236**, 3088–3099 (2007).
53. Ellett, F., Pase, L., Hayman, J. W., Andrianopoulos, A. & Lieschke, G. J. mpeg1 promoter transgenes direct macrophage-lineage expression in zebrafish. *Blood* **117**, e49–e56 (2011).
54. Mathias, J. R., Zhang, Z., Saxena, M. T. & Mumm, J. S. Enhanced cell-specific ablation in zebrafish using a triple mutant of *Escherichia coli* nitroreductase. *Zebrafish* **11**, 85–97 (2014).
55. Chen, S., Chiu, C. N., McArthur, K. L., Fetcho, J. R. & Prober, D. A. TRP channel mediated neuronal activation and ablation in freely behaving zebrafish. *Nat. Methods* **13**, 147–150 (2016).
56. Shiau, C. E., Monk, K. R., Joo, W. & Talbot, W. S. An anti-inflammatory NOD-like receptor is required for microglia development. *Cell Rep.* **5**, 1342–1352 (2013).
57. Almeida, R. & Lyons, D. Oligodendrocyte development in the absence of their target axons in vivo. *PLoS ONE* **11**, e0164432 (2016).
58. Li, L., Jin, H., Xu, J., Shi, Y. & Wen, Z. Irf8 regulates macrophage versus neutrophil fate during zebrafish primitive myelopoiesis. *Blood* **117**, 1359–1369 (2011).
59. Kucenas, S., Wang, W.-D., Knapik, E. W. & Appel, B. A selective glial barrier at motor axon exit points prevents oligodendrocyte migration from the spinal cord. *J. Neurosci.* **29**, 15187–15194 (2009).
60. Wang, Y. et al. Accurate quantification of astrocyte and neurotransmitter fluorescence dynamics for single-cell and population-level physiology. *Nat. Neurosci.* **22**, 1936–1944 (2019).
61. Legland, D., Arganda-Carreras, I. & Andrey, P. MorphoLibJ: integrated library and plugins for mathematical morphology with ImageJ. *Bioinformatics* **32**, 3532–3534 (2016).
62. Longair, M. H., Baker, D. A. & Armstrong, J. D. Simple neurite tracer: open source software for reconstruction, visualization and analysis of neuronal processes. *Bioinformatics* **27**, 2453–2454 (2011).

Acknowledgements

Author contributions
A.N.H. and B.A. conceptualized the project. A.N.H. designed and performed the experiments and collected and analyzed the data. A.N.H. wrote, and B.A. edited, the manuscript.

Competing interests
The authors declare no competing interests.

Additional information
Extended data is available for this paper at https://doi.org/10.1038/s41593-020-0654-2.

Supplementary information is available for this paper at https://doi.org/10.1038/s41593-020-0654-2.

Correspondence and requests for materials should be addressed to B.A.

Peer review information *Nature Neuroscience* thanks Marie-Ève Tremblay and the other, anonymous, reviewer(s) for their contribution to the peer review of this work.

Reprints and permissions information is available at www.nature.com/reprints.
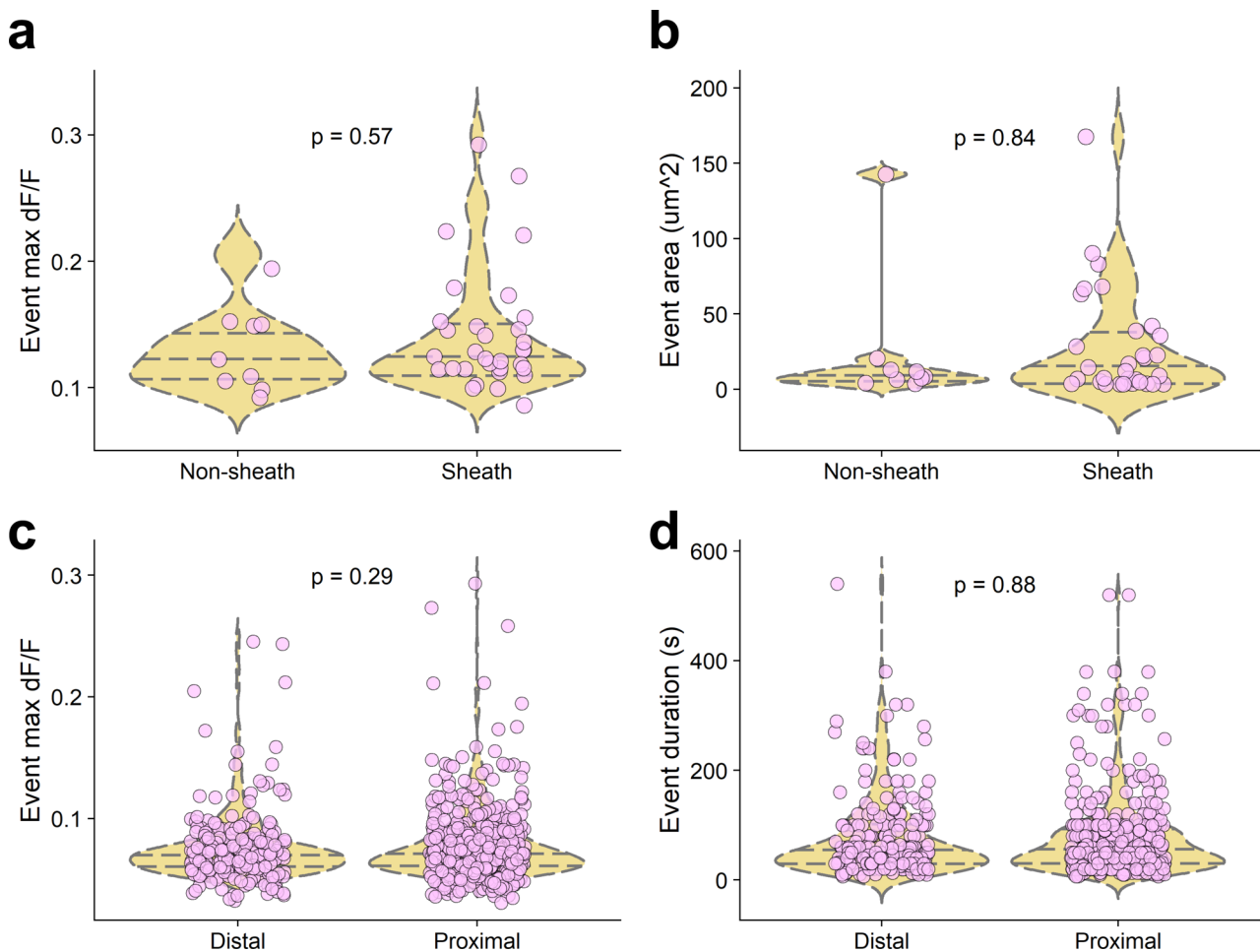
Extended Data Fig. 1 | Calcium events in microglial processes contacting myelin sheaths compared to processes not contacting sheaths and comparison with event proximity to the soma. a, b, Max dF/F (**a**) and event area (**b**) for large events (dF/F >0.1, area > 3 μm²) at non-sheath-contacting and sheath-contacting processes of microglia at 4 d.p.f. in *Tg(mpeg1.1:GCaMP6s-CAAX; sox10:mRFP)* larvae. Wilcoxon rank-sum test, n=41 events from 9 microglia in 9 fish. **c, d,** To distinguish if distance from cell soma is responsible for sheath-contacting vs non-contacting event differences, we split 645 events that occurred in 31 cells (31 fish) into distal and proximal halves and assessed event dF/F (**c**) and duration (**d**); ns by Wilcoxon rank-sum test.
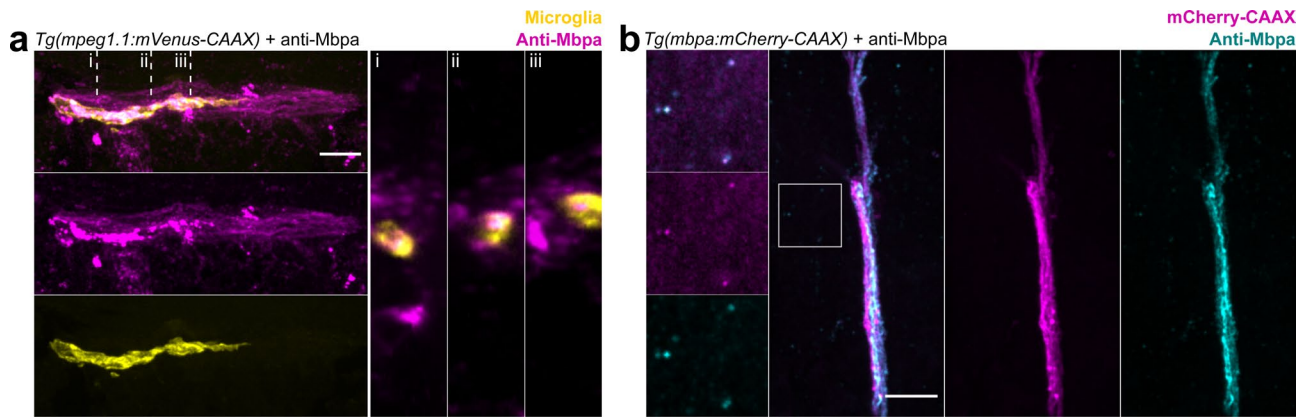
Extended Data Fig. 2 | Anti-Mbpa detects myelin within microglia. a, Coronal section of *Tg(mpeg1.1:mVenus-CAAX)* 6 d.p.f. larval spinal cord stained with anti-Mbpa to detect myelin. Note anti-Mbpa inclusions (magenta) within microglia (yellow) in orthogonal views (right panels) taken at the locations marked (i), (ii), (iii). **b**, Coronal section of *Tg(mbpa:mCherry-CAAX)* 6 d.p.f. tectal commissure stained with anti-Mbpa (cyan) to detect myelin. Oligodendrocyte membrane (mCherry-CAAX) colocalizes with anti-Mbpa (cyan), both in the intact commissure and as a limited amount of extracellular debris (inset). Scale bars, 10 μm.

a

myrf:mScarlet-CAAX
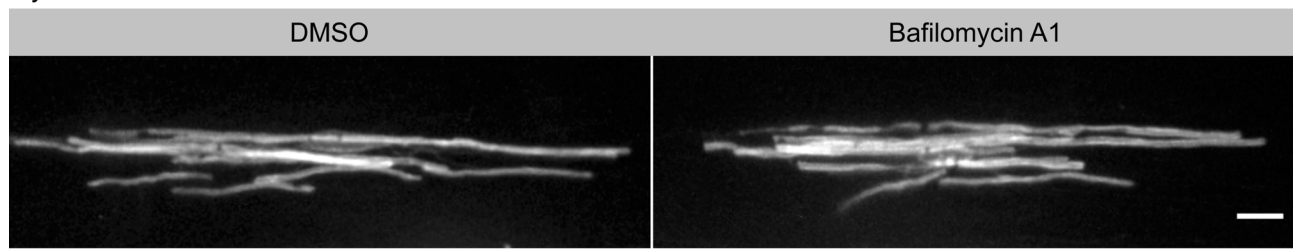
b
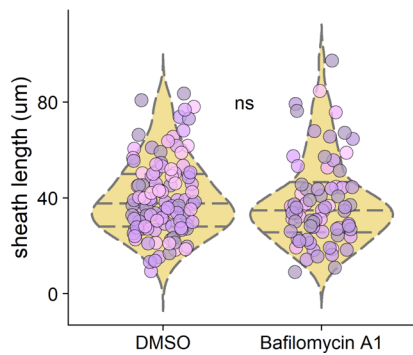
c
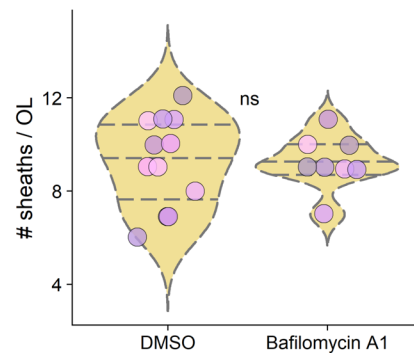
Extended Data Fig. 3 | Acute treatment of larvae with bafilomycin A1 does not affect oligodendrocyte myelination. a, Representative individual oligodendrocytes in transient-transgenic *myrf*:mScarlet-CAAX expressing larvae treated with bafilomycin A1 or DMSO. Scale bar, 10 μm. **b**, **c**, Quantification of sheath length and number of oligodendrocytes in each treatment group. n=12 larvae/12 fish (DMSO), 8 larvae/8 fish (bafilomycin A1). Data in (**b**) and (**c**) analyzed by Wilcoxon rank-sum test.
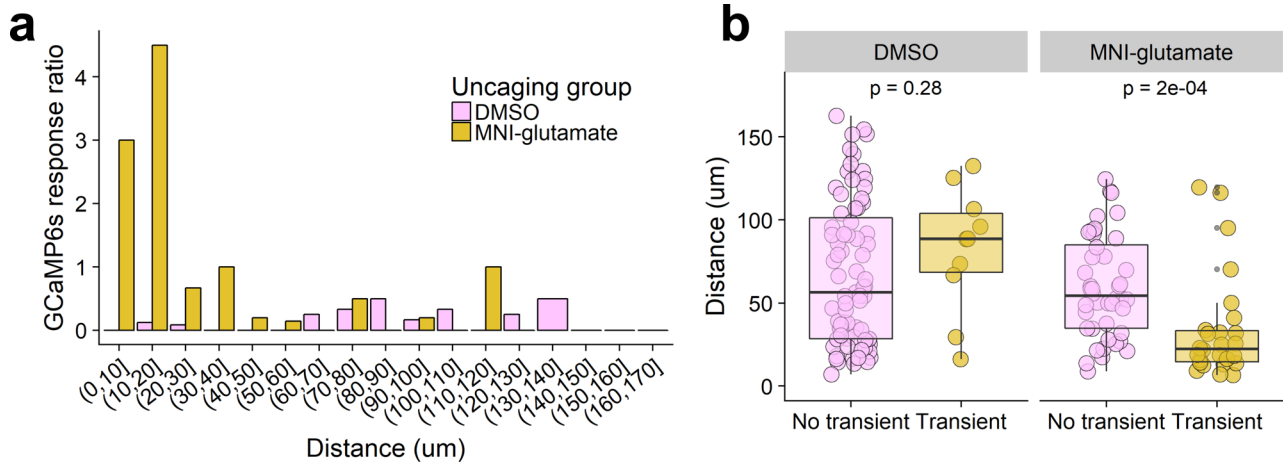
Extended Data Fig. 4 | Glutamate uncaging evokes Ca^{2+} transients most reliably in neurons located < 20 μm away from the uncaging site. a, Ratio of Ca^{2+} transient-experiencing neurons to those without transients binned in 10 μm bins from the uncaging site. **b**, Distance of neurons with Ca^{2+} transients (defined as dF/F>0.5) or no transients from the uncaging point in larvae treated with DMSO or MNI-glutamate, analyzed by Wilcoxon rank-sum test (n=fish/neurons, n=5/85 DMSO, 9/70 MNI-glutamate).
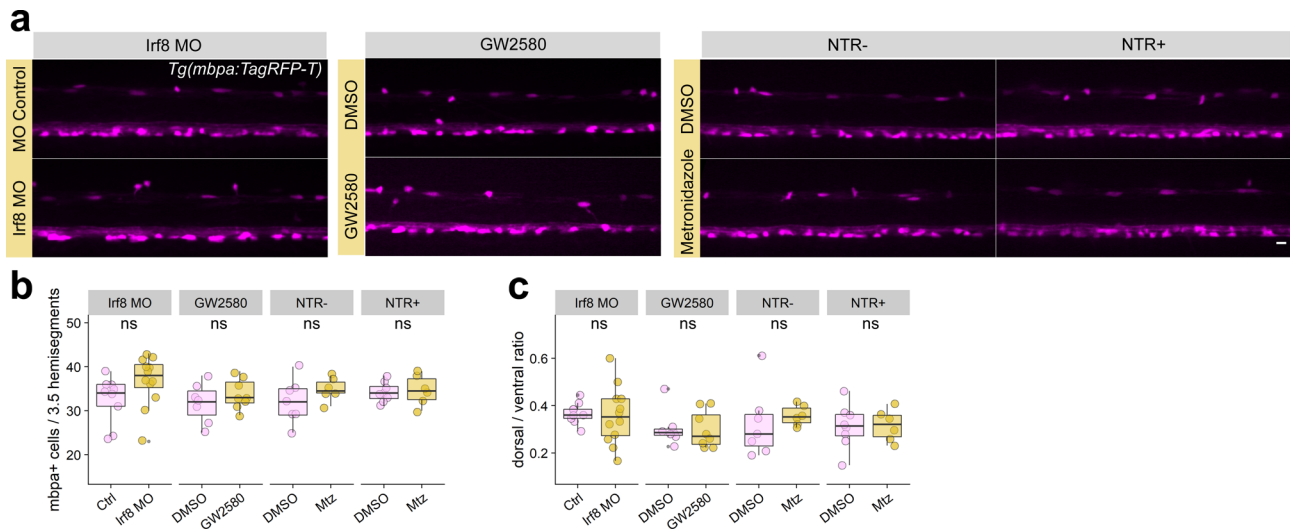
Extended Data Fig. 5 | Microglia ablation does not change oligodendrocyte number or distribution. a, Max projection images of hemi-spinal cords in 4 d.p.f. *Tg(mbpa:TagRFP-T)* larvae in each microglia ablation group and controls. Scale bar, 10 μm. **b**, **c**, Total number (**b**) and dorsal/ventral distribution (**c**) of oligodendrocytes per 3.5 hemisegments in each ablation group paired with corresponding controls, analyzed by Wilcoxon rank sum test (n=fish/oligodendrocytes, groups left to right, n=9/293, 12/442, 7/222, 8/271, 7/225, 6/209, 8/274, 6/208).

Neuronal activity high:
Microglia contact neuronal cell bodies,
less available to phagocytose myelin
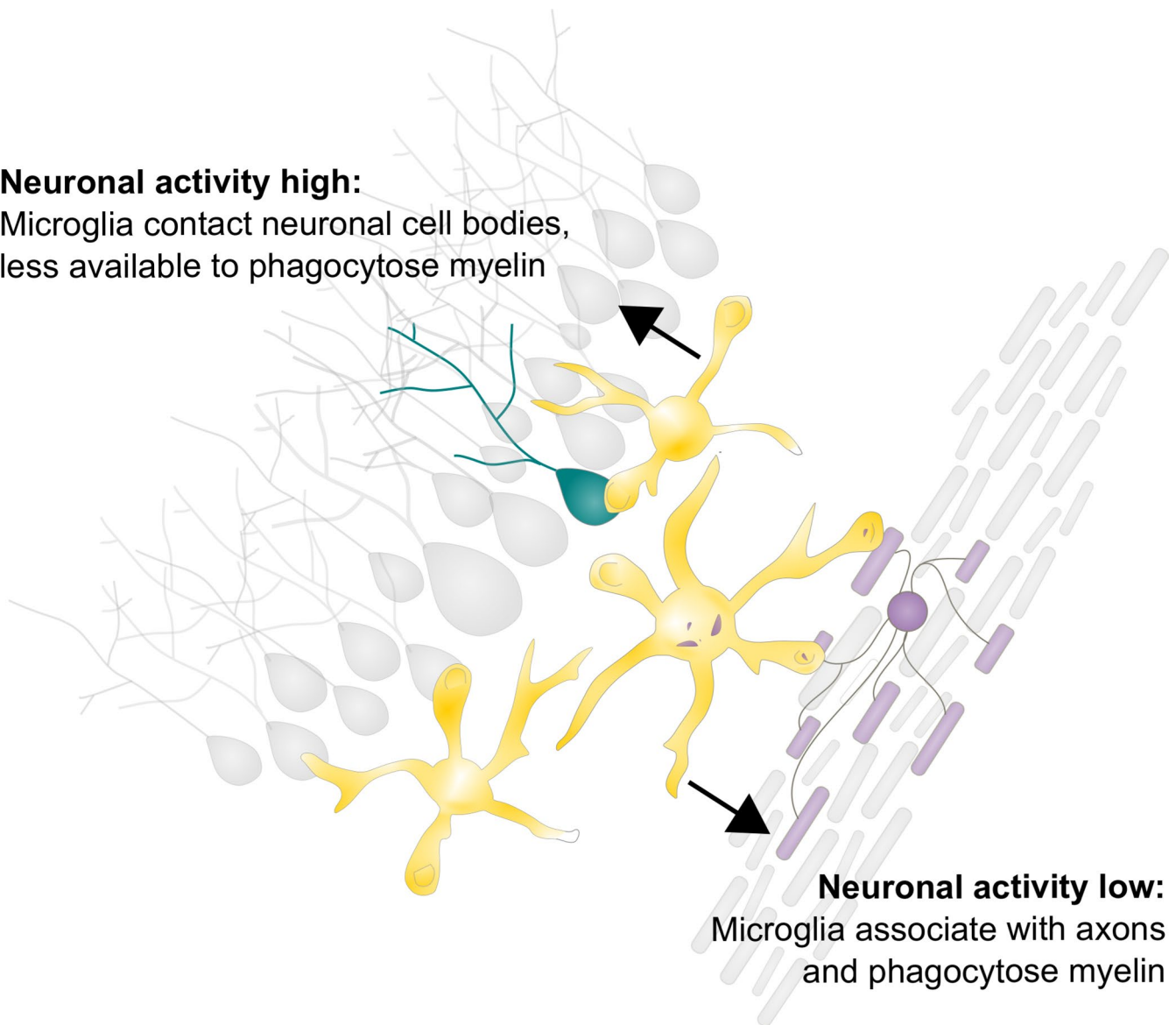
Neuronal activity low:
Microglia associate with axons
and phagocytose myelin

Extended Data Fig. 6 | Working model of activity-regulated myelin phagocytosis by microglia. Microglia phagocytose myelin to regulate myelin sheath number and targeting. Neuronal activity attracts microglia to contact neuronal cell bodies and reduces the amount of myelin that microglia can phagocytose, whereas reductions in neuronal activity promote myelin phagocytosis from axons.

nature research

Corresponding author(s):	Bruce Appel
Last updated by author(s):	4/18/2020

Reporting Summary

Nature Research wishes to improve the reproducibility of the work that we publish. This form provides structure for consistency and transparency in reporting. For further information on Nature Research policies, see Authors & Referees and the Editorial Policy Checklist.

Statistics

For all statistical analyses, confirm that the following items are present in the figure legend, table legend, main text, or Methods section.

n/a	Confirmed	
☐	☒	The exact sample size (*n*) for each experimental group/condition, given as a discrete number and unit of measurement
☐	☒	A statement on whether measurements were taken from distinct samples or whether the same sample was measured repeatedly
☐	☒	The statistical test(s) used AND whether they are one- or two-sided *Only common tests should be described solely by name; describe more complex techniques in the Methods section.*
☒	☐	A description of all covariates tested
☐	☒	A description of any assumptions or corrections, such as tests of normality and adjustment for multiple comparisons
☐	☒	A full description of the statistical parameters including central tendency (e.g. means) or other basic estimates (e.g. regression coefficient) AND variation (e.g. standard deviation) or associated estimates of uncertainty (e.g. confidence intervals)
☐	☒	For null hypothesis testing, the test statistic (e.g. *F*, *t*, *r*) with confidence intervals, effect sizes, degrees of freedom and *P* value noted *Give P values as exact values whenever suitable.*
☒	☐	For Bayesian analysis, information on the choice of priors and Markov chain Monte Carlo settings
☒	☐	For hierarchical and complex designs, identification of the appropriate level for tests and full reporting of outcomes
☒	☐	Estimates of effect sizes (e.g. Cohen's *d*, Pearson's *r*), indicating how they were calculated

Our web collection on statistics for biologists contains articles on many of the points above.

Software and code

Policy information about availability of computer code

Data collection	Morphological segmentation data were collected with the Fiji plugin MorphoLibJ. Sheath length and number data were collected with the Fiji plugin Simple Neurite Tracer. Calcium and membrane transients were collected with the Fiji plugin AQuA. Sheath retraction vs engulfment analysis was performed with the Fiji plugin ImageCalculator.
Data analysis	All statistical analyses were performed in R with RStudio (3.4.1) with the package ggpubr (Kassambara, 2017)

For manuscripts utilizing custom algorithms or software that are central to the research but not yet described in published literature, software must be made available to editors/reviewers. We strongly encourage code deposition in a community repository (e.g. GitHub). See the Nature Research guidelines for submitting code & software for further information.

Data

Policy information about availability of data

All manuscripts must include a data availability statement. This statement should provide the following information, where applicable:

- Accession codes, unique identifiers, or web links for publicly available datasets
- A list of figures that have associated raw data
- A description of any restrictions on data availability

All data is available in the manuscript or in the supplementary materials.

Field-specific reporting

Please select the one below that is the best fit for your research. If you are not sure, read the appropriate sections before making your selection.

☒ Life sciences ☐ Behavioural & social sciences ☐ Ecological, evolutionary & environmental sciences

For a reference copy of the document with all sections, see nature.com/documents/nr-reporting-summary-flat.pdf

Life sciences study design

All studies must disclose on these points even when the disclosure is negative.

Sample size	Sample sizes were determined based on similar experiments carried out in larval zebrafish, where numbers of analyzed cells/sheaths were sufficient to detect changes in myelination (Hines et al, 2015; Mensch et al, 2015; Czopka et al, 2013). When experiments had not previously been carried out by other groups (inclusion analysis, for example), we used sample sizes from experiments of similar design (the number of microglia analyzed for inclusions is based on the number of OLs needed for ensheathment analysis, as previously reported). In every case, after data were analyzed, no replicates were added or excluded to change sample size of any group.
Data exclusions	No data were excluded from analyses.
Replication	All attempts at replication were successful. Individual cells analyzed were largely derived from independent animals (1-2 cells/larvae), collected from 3-5 different clutches and analyzed independently.
Randomization	Larvae (sibling clutch-mates) were randomly allocated into groups at the 1-2 cell stage for injection or later drug treatment. Zebrafish sex is not yet determined at the stages analyzed in our study and was not a factor.
Blinding	Groups were not blinded at acquisition, but similar regions were imaged in all groups (spinal cord over the yolk sac extension; dorsal optic tectum, larvae mounted laterally in both cases). We performed all image analysis blinded using the Fiji plugin Lab-utility-plugins/blind-files.

Reporting for specific materials, systems and methods

We require information from authors about some types of materials, experimental systems and methods used in many studies. Here, indicate whether each material, system or method listed is relevant to your study. If you are not sure if a list item applies to your research, read the appropriate section before selecting a response.

Materials & experimental systems

n/a	Involved in the study
☐	☒ Antibodies
☒	☐ Eukaryotic cell lines
☒	☐ Palaeontology
☐	☒ Animals and other organisms
☒	☐ Human research participants
☒	☐ Clinical data

Methods

n/a	Involved in the study
☒	☐ ChIP-seq
☒	☐ Flow cytometry
☒	☐ MRI-based neuroimaging

Antibodies

Antibodies used	Rabbit anti-Mbpa (Open Biosystems, e9043, 1:200 dilution); Alexa Fluor 647 goat anti-rabbit antibody (Jackson ImmunoResearch, 111-605-003, 1:200 dilution)
Validation	Rabbit anti-Mbpa antibody is a custom-made antibody generated against zebrafish Mbpa that was previously published and validated for immunohistochemistry in zebrafish (Kucenas et al, 2009, J Neurosci).

Animals and other organisms

Policy information about studies involving animals; ARRIVE guidelines recommended for reporting animal research

Laboratory animals	Zebrafish (Danio rerio), AB strain, age 4-8 days post fertilization, were used for all experiments. Zebrafish sex is not yet determined at these stages and was thus not a factor. Animals were all either transgenic or transient-transgenic to label cells of interest and no mutant strains were used.
Wild animals	No wild animals
Field-collected samples	No field-collected samples

Ethics oversight | All animal work was approved by the Institutional Animal Care and Use Committee at the University of Colorado.

Note that full information on the approval of the study protocol must also be provided in the manuscript.